ESAIM: M2AN 51 (2017) 679–706
DOI: 10.1051/m2an/2016033

ESAIM: Mathematical Modelling and Numerical Analysis
www.esaim-m2an.org

A GENERALIZED MIMETIC FINITE DIFFERENCE METHOD AND TWO-POINT FLUX SCHEMES OVER VORONOI DIAGRAMS

Omar Al-Hinai[1], Mary F. Wheeler[1] and Ivan Yotov[2]

Abstract. We develop a generalization of the mimetic finite difference (MFD) method for second order elliptic problems that extends the family of convergent schemes to include two-point flux approximation (TPFA) methods over general Voronoi meshes, which are known to satisfy the discrete maximum principle. The method satisfies a modified consistency condition, which utilizes element and face weighting functions. This results in shifting the points on the elements and faces where the pressure and the flux are most accurately approximated. The flux bilinear form is non-symmetric in general, although it reduces to a symmetric form in the case of TPFA. It can be defined as the L^2-inner product of vectors in two $H(\Omega;\mathrm{div})$ discrete spaces, which are constructed via suitable lifting operators. A specific construction of such lifting operators is presented on rectangles. We note that a different choice is made for test and trial spaces, therefore the method can be viewed as a $H(\Omega;\mathrm{div})$-conforming Petrov–Galerkin Mixed Finite Element method. We prove first-order convergence in pressure and flux, and superconvergence of the pressure under further restrictions. We present numerical results that support the theory.

Mathematics Subject Classification. 65M60, 65N08, 76S05.

Received September 5, 2015. Revised April 13, 2016. Accepted May 5, 2016.

1. Introduction

Finite Volume Methods (FVM) are among the most widely used techniques for the numerical solution of partial differential equations, especially those governing fluid flow problems [28]. The popularity of FVM is due to the fact that they are locally conservative by construction, fast and robust for a wide range of problems, and can preserve the maximum principle. FVM can be defined over a wide variety of mesh types, including triangular/tetrahedral, quadrilateral/hexahedral and Voronoi type meshes [6, 28, 47]. The reader is referred to [25, 26] for work on unstructred grids and full tensor permeabilities, and [1] for distorted grids and multipoint flux approximations (MPFA).

FVM can be related to other discretization methods such as the Finite Difference Method and the Finite Element Method. Of note is the connection established in [50] for mixed finite element (MFE) methods, where the lowest order Raviart–Thomas element (RT_0) [49] over rectangles was shown to be equivalent to cell-centered

Keywords and phrases. Mimetic finite difference, finite volume methods, discrete maximum principle, polyhedral meshes, Voronoi diagrams.

[1] Institute for Computational Engineering and Sciences, The University of Texas at Austin, 201 East 24th Street, Austin, TX 78712, USA. ohinai@gmail.com; mfw@ices.utexas.edu

[2] Department of Mathematics, University of Pittsburgh, Pittsburgh, PA 15260, USA. yotov@math.pitt.edu

finite differences. The technique demonstrated how to reduce the number of degrees of freedom for RT_0 and produce a linear symmetric positive definite system for the pressure variable. This connection enabled a proof of convergence for FVM based on the theory of MFE methods [55]. Many authors have subsequently built on these ideas, producing further connections and more theoretical results. An extension for full-tensor coefficients was developed in [4, 5]. Connections between MFE methods and FVM on simplicial meshes were established in [8, 54]. Superconvergence for both the scalar and vector unknowns has been shown in [22, 27, 46]. Further extensions include the use of the lowest order Brezzi-Douglas-Marini element (BDM_1) [13] for connecting MFE methods with MPFA [35, 56, 57]. A similar connection based on broken RT_0 elements was developed in [38, 39].

While there has been success in demonstrating the connection between MFE methods and FVM, some types of FVM have not been connected with MFE methods. An example is the two-point flux approximation (TPFA) over Voronoi diagrams and K-orthogonal grids (grids aligned with the eigenvectors of the permeability tensor) [28]. Connecting such a method to MFE methods would require the construction of discrete $H(\Omega;\mathrm{div})$ spaces over convex polyhedra with an arbitrary number of faces. While such spaces have been constructed via a local triangulation of the cells [40], it remains uncertain if such an approach can be reduced to TPFA. The work done in [14, 15] on the Mimetic Finite Difference method (MFD) opens up some possibilities. The authors of [14] use theoretical tools from MFE methods to demonstrate convergence of the MFD method over a very general set of polyhedral cells. This is accomplished by avoiding the explicit construction of the velocity variable on the interior, and directly solving for flux degrees of freedom on the faces of the cells. The definition of the MFD method in [15] allowed for a reduction to TPFA for the case of regular polyhedra and rectangles. Later work in [23] extended the MFD method to include TPFA for acute triangular cells. The authors of [41] provided generalizations of the MFD method that included TPFA over centroidal Voronoi diagrams as well as MPFA methods over general polyhedra; see also related work in [37].

The objective of our work is to provide a further generalization of the MFD method that allows for TPFA type methods over general Voronoi diagrams. TPFA schemes on Voronoi diagrams are ubiquitous in reservoir simulation, where they are used to mesh around horizontal and multi-lateral wells, to generate radial and honeycomb meshes, as well as local refinements that satisfy the discrete maximum principle, see *e.g.* Schlumberger's Eclipse [52] and Aramco's GigaPOWERS [30]. They are also used in major hydrology simulators such as Berkeley Lab's TOUGH [10, 29] and geology codes such as MODFLOW-USG developed by the USGS [48]. Therefore, being able to connect these schemes to MFD methods has important practical applications. In particular, the theoretical framework for analysis of MFD methods can be utilized to establish convergence and superconvergence results and to develop higher-order postprocessing, *a posteriori* error estimation, and adaptive mesh refinement for FVM over general Voronoi diagrams. From a point of view of MFD methods, the reduction to TPFA results in improved efficiency of the method, as well as solutions that satisfy the maximum principle.

To establish the connection between MFD methods and TPFA methods over general Voronoi diagrams, we propose a modified form of the consistency condition ($S2$) in [14], which we call here ($\widetilde{S2}$). The modification is inspired by the consistency conditions proposed by [23] and [41] and utilizes element and face weighting functions. This results in shifting the points on the elements and faces where the pressure and the flux are most accurately approximated. Our formulation results in a new extended family of MFD methods, parametrized by the element and face weighting functions. The flux bilinear form is non-symmetric in general, although it reduces to a symmetric form in the case of TPFA when the element points are the Voronoi generating points and the face points are the Voronoi bisection points. It is also symmetric when the face weighting functions are set to one, *i.e.*, the face points are the face centroids. The flux bilinear form can be defined as the L^2-inner product of vectors in two $H(\Omega;\mathrm{div})$ discrete spaces, which are constructed via suitable lifting operators. A specific construction of such lifting operators is presented on rectangles. We note that a different choice is made for test and trial spaces, therefore the method can be viewed as a $H(\Omega;\mathrm{div})$-conforming Petrov–Galerkin MFE method.

We demonstrate the stability of the new family of methods as well as the convergence in the velocity and pressure unknowns. As it is typical in MFD analysis, convergence is established in a discrete norm for the error between the numerical solution and an interpolant of the true solution. Due the use of weighting functions,

we consider both standard and weighted interpolants for the pressure and velocity and establish first-order convergence for the two variables for both types of interpolants. Furthermore, we demonstrate superconvergence in the pressure variable for the weighted interpolant, which corresponds to second order approximation of the pressure at shifted points within the elements. We note that existing pressure superconvergence results for MFD methods are limited to symmetric formulations, see *e.g.* [14,41]. To the best of our knowledge, we obtain the first pressure superconvergence result for non-symmetric MFD methods. The techniques developed in this paper could be used to establish pressure superconvergence for MPFA methods on general polyhedra, which are inherently non-symmetric. We further note that the pressure superconvergence for the weighted interpolant can be explored to reconstruct a second-order accurate piecewise linear approximation of the pressure. This is outside the scope of the paper and will be studied in the future.

In recent years, there have been a number of developments in the area of discretization methods defined over polygonal and polyhedral meshes. The Virtual Element Method (VEM) [19], which is strongly related to the MFD method, is generalizable to higher-order discretizations. A mixed VEM has been developed in [16], which is closely related to the mixed version of MFD methods studied in this paper. The Gradient Schemes [24] provide a very general framework that is based on constructing a discrete gradient operator. Similar ideas are explored in the Weak Galerkin method [45], the Hybridizable Discontinuous Galerkin method [2,18], as well as the Hybrid High-Order method [21]. Many of these methods require the addition of scalar unknowns (Lagrange multipliers) at the faces of the mesh, while such an addition remains optional for our approach. More importantly, all of the above mentioned methods are symmetric, while our formulation is in general non-symmetric, due to the introduction of the weighting functions. Unlike the above mentioned methods, this extra flexibility provides a formulation that reduces to a convergent finite volume method on general Voronoi diagrams. Furthermore, the extra flexibility of shifting points within the elements and along the faces can be explored to improve the solution accuracy near singularities or to develop methods that satisfy the discrete maximum principle, similar to the approach of M-adaptation for MFD methods [33]. A numerical experiment illustrating that shifting face points can lead to a more accurate flux along a high permeability streak is presented in the numerical section.

The rest of the paper is organized as follows. In Section 2 we define the new generalized form of the MFD method and provide the basic assumptions and definitions used in this work. The stability of the new method is provided in Section 2.1, which is followed by first-order convergence proofs for velocity in Section 2.2 and pressure in Section 2.3. Superconvergence of the pressure is presented in Section 2.4, which includes superconvergence with special quadrature. Novel $H(\Omega;\mathrm{div})$ shape functions that satisfy the superconvergence criteria for rectangular grids are presented in Section 2.4.1. We then discuss matrix construction for the general case in Section 3, and the relation to TPFA schemes on Voronoi grids in Section 4. Numerical results confirming the theory and illustrating the advantage of the ability to shift points are presented in Section 5.

2. A Generalized MFD method

Consider the homogeneous Dirichlet problem written in mixed form,

$$u = -K\nabla p, \quad \nabla \cdot u = f \quad \text{in } \Omega, \quad p = 0 \quad \text{on } \partial\Omega. \tag{2.1}$$

In porous media flow, u is Darcy velocity, p is pressure and K is the permeability tensor. The domain $\Omega \subset \mathbb{R}^d$ $(d = 2, 3)$ is assumed to be polyhedron with Lipschitz boundaries and is divided into a non-overlapping, conformal partition $\mathcal{T}_h$ of elements E. In three dimensions, E is a polyhedron with planar polygonal faces. We follow the standard assumptions for the mesh used in previous work [14,41]. That is, elements and faces are shape-regular and non-degenerate, elements are star-shaped polyhedra, and faces are star-shaped polygons. Let N_Q be the total number of elements in the mesh and N_X be the total number of faces in the mesh. Let $|E|$ denote the volume of E and h_E be the diameter of E. We define $h = \max_{\{E\in\mathcal{T}_h\}} h_E$. For each face e, let $|e|$ be the area, n^e is a fixed unit normal, and n^e_E is the unit normal to face e pointing out of element E. For each element E, k_E represents the number of faces. We note that the mesh assumptions imply that

$$|E| \sim h_E^d \text{ and } |e| \sim h_E^{d-1}. \tag{2.2}$$

Let the space of discrete pressures $Q_h \subset \mathbb{R}^{N_Q}$ and fluxes $X_h \subset \mathbb{R}^{N_X}$ be defined, respectively, as

$$Q_h = \{q_h = \{q_E\}_{E\in\mathcal{T}_h} : q_E \in \mathbb{R}\}, \quad X_h = \{v_h = \{v_E^e\}_{E\in\mathcal{T}_h}^{e\in\partial E} : v_E^e \in \mathbb{R},\ v_{E_a}^e + v_{E_b}^e = 0\},$$

where E_a and E_b share a face e. Each degree of freedom q_E represents the pressure on element E, while each degree of freedom v_E^e represents the flux normal to face e outward to E. The continuity of flux condition $v_{E_a}^e + v_{E_b}^e = 0$ implies a single velocity degree of freedom per face e.

In the following, we make use of the usual notation for Lebesgue spaces $L^p(\Omega)$, Sobolev spaces $W^{k,p}(\Omega)$ and Hilbert spaces $H^k(\Omega)$, see [11]. For $q \in L^1(\Omega)$, define a projection operator on Q_h as

$$(q^I)_E = \frac{1}{|E|}\int_E q\,\mathrm{d}V. \tag{2.3}$$

For $v \in (L^s(\Omega))^d$, $s > 2$ and $\nabla\cdot v \in L^2(\Omega)$, define the projection operator on X_h as

$$(v^I)_E^e = \frac{1}{|e|}\int_e v\cdot n_E^e\,\mathrm{d}S. \tag{2.4}$$

Let the permeability tensor K be symmetric and positive definite, and let

$$K_{ij} \in W^{1,\infty}(\Omega). \tag{2.5}$$

Let $\bar{K}_E$ denote a constant tensor over E such that

$$\max_{ij}\|K_{ij} - \bar{K}_{E,ij}\|_{L^\infty(E)} \le Ch_E, \tag{2.6}$$

$$\max_{ij}\|K_{ij}^{-1} - \bar{K}_{E,ij}^{-1}\|_{L^\infty(E)} \le Ch_E. \tag{2.7}$$

Throughout the paper, C denotes a generic positive constant independent of h.

Following the standard steps of the MFD method [43], we define the discrete divergence operator $\mathcal{DIV} : X_h \to Q_h$ as

$$(\mathcal{DIV}\,v_h)_E = \mathcal{DIV}\,v_E := \frac{1}{|E|}\sum_{e\in\partial E} v_E^e|e|. \tag{2.8}$$

We have from (2.3), (2.4), (2.8), and the divergence theorem that,

$$(\mathcal{DIV}\,v^I)_E = (\nabla\cdot v)_E^I. \tag{2.9}$$

Next, define the scalar inner product as

$$[p_h, q_h]_{Q_h} := \sum_{E\in\mathcal{T}_h} p_E q_E|E|.$$

The flux bilinear form is defined as

$$[u_h, v_h]_{X_h} := \sum_{E\in\mathcal{T}_h}[u_E, v_E]_E = \sum_{E\in\mathcal{T}_h} v_E^T\mathbf{M}_E u_E, \tag{2.10}$$

where $u_E \in \mathbb{R}^{k_E}$ is the vector with components u_E^e and $\mathbf{M}_E \in \mathbb{R}^{k_E\times k_E}$ is a given matrix. We discuss the construction of $\mathbf{M}_E$ in Section 3. We assume that $[\cdot,\cdot]_{X_h}$ satisfies:

(*S*1) (*Stability*). There exist two positive constants, s_* and S^*, such that, for all $E \in \mathcal{T}_h$ and $\xi \in \mathbb{R}^{k_E}$,

$$s_*|E|\xi^T\xi \le \xi^T\mathbf{M}_E\xi \le S^*|E|\xi^T\xi, \tag{2.11}$$

and

$$\xi^T \mathbf{M}_E^T \mathbf{M}_E \xi \leq (S^*)^2 |E|^2 \xi^T \xi. \tag{2.12}$$

$(\widetilde{S2})$ (*Consistency*). For every element $E \in \mathcal{T}_h$, for every linear function q^1 on E, and for every $v_E \in X_h(E)$,

$$[(\bar{K}_E \nabla q^1)_E^I, v_E]_E = \sum_{e \in \partial E} v_E^e \int_e w_e q^1 \, \mathrm{d}S - \int_E w_E q^1 \mathcal{D}\mathcal{I}\mathcal{V} \, v_E \, \mathrm{d}V, \tag{2.13}$$

where the function $w_E : E \to \mathbb{R}$ satisfies

$$\int_E w_E \, \mathrm{d}V = |E|, \quad \int_E g w_E \, \mathrm{d}V = |E| x_E, \tag{2.14}$$

where x_E is a point in E and $g : \mathbb{R}^d \to \mathbb{R}^d$ is the linear function $g(x, y, z) = (x, y, z)^T$, and where the function $w_e : e \to \mathbb{R}$ satisfies,

$$\int_e w_e \, \mathrm{d}S = |e|, \quad \int_e g w_e \, \mathrm{d}S = |e| x_e, \tag{2.15}$$

where x_e is a point on the plane of e and g is the linear function defined on Cartesian coordinates (x, y) in the plane of e as $g(x, y) = (x, y)^T$. Note that the point x_e may lie outside of e. The original MFD is recovered when $w_E = 1$ and $w_e = 1$, in which case $x_E = C_E$, the centroid of cell E, and $x_e = C_e$, the centroid of face e. We require that the functions w_e and w_E be bounded by positive constants independent of the mesh,

$$\max_{E \in \mathcal{T}_h} \|w_E\|_{L^\infty(E)} \leq w_E^{\max}, \quad \max_{E \in \mathcal{T}_h} \max_{e \in \partial E} \|w_e\|_{L^\infty(e)} \leq w_e^{\max}.$$

Remark 2.1. The addition of weighting functions to the integrals was inspired by the modification suggested in [23]. However, the form in [23] only weighted the integral over the volume, while in this work we weight both the volume and the face integrals. The work in [41] modified the integral over the faces by integrating over a subset of the face. Our work differs by allowing further freedom in point selection on the face, as well as combining the weight over the volume as mentioned.

Define a discrete gradient operator $\mathcal{G} : Q_h \to X_h$ as the adjoint of $\mathcal{D}\mathcal{I}\mathcal{V}$,

$$[\mathcal{G} \, p_h, u_h]_{X_h} = -[p_h, \mathcal{D}\mathcal{I}\mathcal{V} \, u_h]_{Q_h}. \tag{2.16}$$

The numerical method can be represented in a "weak" saddle-point form. That is, find $u_h \in X_h$ and $p_h \in Q_h$ such that

$$[u_h, v_h]_{X_h} - [p_h, \mathcal{D}\mathcal{I}\mathcal{V} \, v_h]_{Q_h} = 0, \qquad \forall v_h \in X_h, \tag{2.17}$$

$$[\mathcal{D}\mathcal{I}\mathcal{V} \, u_h, q_h]_{Q_h} = [f^I, q_h]_{Q_h}, \qquad \forall q_h \in Q_h. \tag{2.18}$$

Remark 2.2. The theoretical results presented here follow the exposition found in [41]. We have made modifications when necessary to adapt to the modified consistency condition $(\widetilde{S2})$. Since the stability analysis does not depend on the consistency condition $(\widetilde{S2})$, the stability results from [14] and [41] still hold.

2.1. Stability analysis

The analysis follows the classical approach to stability of mixed methods. We start by defining the following norms over the pressure and flux spaces,

$$\|v_h\|_{X_h}^2 = [v_h, v_h]_{X_h}, \quad \|q_h\|_{Q_h}^2 = [q_h, q_h]_{Q_h}.$$

The fact that $\|\cdot\|_{X_h}$ is a norm follows from

$$s_*|E| \sum_{e\in\partial E} |v_E^e|^2 \le [v_E, v_E]_E \le S^*|E| \sum_{e\in\partial E} |v_E^e|^2 \quad \forall E \in \mathcal{T}_h, \forall v_E \in X_h(E), \tag{2.19}$$

which is a direct consequence of (2.11) in condition $(S1)$. Note that (2.4) and (2.19) imply that for any $v \in (H^1(E))^d$,

$$\|v^I\|_{X_{h,E}} \le C\|v\|_{(H^1(E))^d}. \tag{2.20}$$

It is easy to see that (2.11) and (2.12) in $(S1)$ imply the continuity of the bilinear form,

$$[u_h, v_h]_{X_h} \le \frac{S^*}{s_*}\|u_h\|_{X_h}\|v_h\|_{X_h}. \tag{2.21}$$

We also define discrete $H(\Omega;\mathrm{div})$ norm

$$\|v_h\|_{\mathrm{div}}^2 = \|v_h\|_{X_h}^2 + \|\mathcal{DIV}\, v_h\|_{Q_h}^2.$$

We clearly have that $\forall q_h \in Q_h$ and $\forall v_h \in X_h$,

$$[q_h, \mathcal{DIV}\, v_h]_{Q_h} \le \|q_h\|_{Q_h}\|v_h\|_{\mathrm{div}}.$$

Let Z_h represent the discrete divergence-free subspace of X_h,

$$Z_h = \{v_h \in X_h \mid [\mathcal{DIV}\, v_h, q_h]_{Q_h} = 0,\ \forall q_h \in Q_h\}.$$

Note that since $\mathcal{DIV}\, v_h \in Q_h$, $v_h \in Z_h$ implies that $\mathcal{DIV}\, v_h = 0$. This immediately implies the coercivity of the flux bilinear operator,

$$[v_h, v_h]_{X_h} = \|v_h\|_{\mathrm{div}}^2 \ \ \forall v_h \in Z_h. \tag{2.22}$$

The inf-sup condition for the bilinear operator $[\cdot\,, \mathcal{DIV}\,\cdot]_{Q_h}$, has been shown in [41].

Theorem 2.3 (inf-sup)**.** *There exists a positive constant β independent of h such that, for any $q_h \in Q_h$,*

$$\sup_{\{v_h\in X_h, v_h\neq 0\}} \frac{[\mathcal{DIV}\, v_h, q_h]_{Q_h}}{\|v_h\|_{\mathrm{div}}} \ge \beta\|q_h\|_{Q_h}. \tag{2.23}$$

The existence and uniqueness of the solution (v_h, p_h) to (2.17)–(2.18) follows from (2.22) and Theorem 2.3, using the general theory for saddle-point problems [12].

2.2. Velocity convergence

In this section we establish a first-order error estimate for the velocity variable. We will utilize an approximation result from [11]: for any element E and $\phi \in H^2(E)$, there exists a linear function ϕ_E^1 such that

$$\|\phi - \phi_E^1\|_{H^k(E)} \le Ch_E^{m-k}|\phi|_{H^m(E)}, \ \ k = 0, 1,\ m = 1, 2. \tag{2.24}$$

We will also utilize the trace inequalities [3]:

$$\forall\, \chi \in H^1(E),\ \|\chi\|^2_{L^2(e)} \leq C\left(h_E^{-1}\|\chi\|^2_{L^2(E)} + h_E|\chi|^2_{H^1(E)}\right), \tag{2.25}$$

$$\forall\, v \in (H^1(E))^d,\ \|v\cdot n_E^e\|^2_{L^2(e)} \leq C\left(h_E^{-1}\|v\|^2_{(L^2(E))^d} + h_E|v|^2_{(H^1(E))^d}\right). \tag{2.26}$$

A combination of (2.24) and (2.25) implies that for any $\phi \in H^2(E)$, there exists a linear function ϕ_E^1 such that

$$\|\phi - \phi_E^1\|^2_{L^2(e)} \leq Ch_E^3|\phi|^2_{H^2(E)}. \tag{2.27}$$

The main result of this section is the following theorem bounding the velocity error.

Theorem 2.4 (Velocity Estimate)**.** *For the exact solution (u,p) of (2.1) and the MFD approximation (u_h,p_h) solving (2.17)–(2.18), assuming that $p\in H^2(\Omega)$, and $u\in(H^1(\Omega))^d$, there exists a positive constant C independent of h, such that*

$$\|u^I - u_h\|_{X_h} \leq Ch(|p|_{H^2(\Omega)} + |p|_{H^1(\Omega)} + |u|_{(H^1(\Omega))^d}). \tag{2.28}$$

Proof. Set $v_h = u^I - u_h$. Note that, using (2.9),

$$\mathcal{DIV}\, v_h = \mathcal{DIV}\,(u^I - u_h) = f^I - f^I = 0.$$

Thus,

$$\|u^I - u_h\|^2_{X_h} = [u^I - u_h, v_h]_{X_h} = [u^I, v_h]_{X_h} - [p_h, \mathcal{DIV}\, v_h]_{Q_h} = [u^I, v_h]_{X_h}. \tag{2.29}$$

Let p^1 be a piecewise linear function such that $p^1|_E = p_E^1$, which is defined in (2.24). By adding and subtracting $(\bar{K}\nabla p^1)^I$,

$$[u^I, v_h]_{X_h} = [u^I + (\bar{K}\nabla p^1)^I, v_h]_{X_h} - [(\bar{K}\nabla p^1)^I, v_h]_{X_h} \equiv I_1 + I_2. \tag{2.30}$$

The analysis of term I_1 is identical to the argument in ([41], Thm. 3.1), implying

$$|I_1| \leq Ch\left(|p|_{H^2(\Omega)} + |p|_{H^1(\Omega)} + |u|_{(H^1(\Omega))^d}\right)\|v_h\|_{X_h}.$$

Since $\mathcal{DIV}\, v_h = 0$, using condition $(\widetilde{S2})$, the expression for I_2 becomes

$$I_2 = -\sum_{E\in\Omega}\sum_{e\in\partial E} v_E^e \int_e w_e p_E^1\, \mathrm{d}S. \tag{2.31}$$

Due to the continuity of p, we can subtract it from each element face in the summation above, obtaining

$$\begin{aligned} |I_2| &= \left|\sum_{E\in\Omega}\sum_{e\in\partial E} v_E^e \int_e w_e(p_E^1 - p)\, \mathrm{d}S\right| \leq \sum_{E\in\Omega}\sum_{e\in\partial E} |e|^{1/2}|w_e^{\max}|\ |v_E^e|\, \|p_E^1 - p\|_{L^2(e)} \\ &\leq C\sum_{E\in\Omega}\left(|E|\sum_{e\in\partial E}|v_E^e|^2\right)^{1/2} h_E|p|_{H^2(E)} \leq Ch|p|_{H^2(\Omega)}\|v_h\|_{X_h}, \end{aligned} \tag{2.32}$$

having used (2.2), (2.27), and (S1). Combining the bounds on I_1 and I_2 with (2.29) and (2.30) gives the desired estimate. □

2.2.1. Weighted projection operator

We also study the operator $u^{I_w} \in X_h$ such that,

$$(u^{I_w})_E^e = \frac{1}{|e|}\int_e w_e u \cdot n_E^e \, \mathrm{d}S.$$

Note that this weighted operator appears in the consistency condition $(\widetilde{S2})$ and therefore it can be expected that the numerical flux u_h provides an improved approximation to u^{I_w}, compared to u^I. We study both errors in the numerical results. We have the following result.

Corollary 2.5. *Under the assumptions of Theorem 2.4,*

$$\|u^{I_w} - u_h\|_{X_h} \leq Ch(|p|_{H^2(\Omega)} + |p|_{H^1(\Omega)} + \|u\|_{(H^1(\Omega))^d}).$$

Proof. The triangle inequality implies

$$\|u^{I_w} - u_h\|_{X_h} \leq \|u^{I_w} - u^I\|_{X_h} + \|u^I - u_h\|_{X_h}.$$

The second term is bounded in Theorem 2.4. Letting,

$$\bar{u} \cdot n_E^e = \int_e u \cdot n_E^e \ \mathrm{d}S,$$

for the first term we have,

$$\begin{aligned}\|u^{I_w} - u^I\|_{X_h}^2 &\leq S^* \sum_E |E| \sum_{e\in\partial E} |(u^{I_w} - u^I)_E^e|^2 = S^* \sum_E \sum_{e\in\partial E} \frac{|E|}{|e|^2}\left(\int_e w_e(u-\bar{u})\cdot n_E^e\right)^2 \\ &\leq S^*(w_e^{\max})^2 \sum_E \sum_{e\in\partial E} \frac{|E|}{|e|}\int_e ((u-\bar{u})\cdot n_E^e)^2 \leq Ch^2\|u\|_{(H^1(\Omega))^d}^2,\end{aligned}$$

where we have used an argument similar to ([56], Lem. 3.14) in the last inequality. Combining the above bounds implies the statement of the corollary. □

2.3. Pressure convergence

We start by defining a weighted operator I_w such that

$$(p^{I_w})_E = \frac{1}{|E|}\int_E w_E p \ \mathrm{d}V.$$

Note that the operator is exact for constant functions. We first establish a pressure estimate with respect to the weighted operator $(\cdot)^{I_w}$. We then establish a bound for the regular projection operator $(\cdot)^I$.

Theorem 2.6. *Let (u,p) be the exact solution to (2.1), and let (u_h,p_h) be the MFD method's numerical approximation (2.17)–(2.18). Assuming that $p \in H^2(\Omega)$ and $u \in (H^1(\Omega))^d$, there exists a constant C independent of h, such that*

$$\|p^{I_w} - p_h\|_{Q_h} \leq Ch(|p|_{H^2(\Omega)} + |p|_{H^1(\Omega)} + |u|_{(H^1(\Omega))^d}). \tag{2.33}$$

Proof. From Theorem 2.3 we know that

$$\|p^{I_w} - p_h\|_{Q_h} \leq \frac{1}{\beta}\sup_{v_h\in X_h, v_h\neq 0} \frac{[\mathcal{DIV}\, v_h, p^{I_w} - p_h]_{Q_h}}{\|v_h\|_{\mathrm{div}}}.$$

Adding and subtracting $(p^1)^{I_w}$, where p^1 is defined in (2.24), we get

$$[\mathcal{DIV}\, v_h, p^{I_w} - p_h]_{Q_h} = [\mathcal{DIV}\, v_h, (p - p^1)^{I_w}]_{Q_h} - [\mathcal{DIV}\, v_h, p_h]_{Q_h} + [\mathcal{DIV}\, v_h, (p^1)^{I_w}]_{Q_h}.$$

Using (2.17) for the second term and condition $(\widetilde{S2})$ for the third term, we have

$$\begin{aligned}[\mathcal{DIV}\, v_h, p^{I_w} - p_h]_{Q_h} &= [\mathcal{DIV}\, v_h, (p - p^1)^{I_w}]_{Q_h} - [u_h, v_h]_{X_h} + \sum_E \sum_e u_E^e \int_e w_e p_E^1 \ \mathrm{d}S - \sum_E [(\bar{K}_E \nabla p_E^1)^I, v_h]_E \\ &\equiv I_3 + I_4 + I_5 + I_6.\end{aligned}$$

We can bound I_3 by

$$\begin{aligned}[\mathcal{DIV}\, v_h, (p - p^1)^{I_w}]_{Q_h} &= \sum_E (\mathcal{DIV}\, v_h, w_E(p - p_E^1))_{L^2(E)} \\ &\le w_E^{\max} \left(\sum_E \|\mathcal{DIV}\, v_h\|_{L^2(E)}^2 \right)^{1/2} \left(\sum_E \|p - p_E^1\|_{L^2(E)}^2 \right)^{1/2} \\ &\le Ch|p|_{H^1(\Omega)} \|\mathcal{DIV}\, v_h\|_{Q_h} \ \text{(using (2.24))}.\end{aligned}$$

Expression I_5 is identical to I_2 in (2.31), implying

$$|I_5| \le Ch|p|_{H^2(\Omega)} \|v_h\|_{X_h}.$$

Taking I_4 and I_6, and adding and subtracting u^I, we have

$$I_4 + I_6 = [(\bar{K}\nabla p^1)^I + u^I, v_h]_{X_h} - [u^I - u_h, v_h]_{X_h} \equiv \tilde{I}_4 + \tilde{I}_6.$$

Expression $\tilde{I}_4$ is identical to I_1 in (2.30), giving the bound

$$|\tilde{I}_4| \le Ch(|p|_{H^2(\Omega)} + |p|_{H^1(\Omega)} + |u|_{(H^1(\Omega))^d}) \|v_h\|_{X_h}.$$

Expression $\tilde{I}_6$ is bounded by the velocity estimate in Theorem 2.4,

$$|\tilde{I}_6| \le C\|u^I - u_h\|_{X_h} \|v_h\|_{X_h} \le Ch(|p|_{H^2(\Omega)} + |u|_{(H^1(\Omega))^d}) \|v_h\|_{X_h}.$$

Combining the bounds on I_3-I_6 gives the desired result. □

We can now derive a bound based on the L^2 projection operator $(\cdot)^I$ defined in (2.3).

Corollary 2.7. *Under the assumptions of Theorem 2.6,*

$$\|p^I - p_h\|_{Q_h} \le Ch(|p|_{H^2(\Omega)} + |p|_{H^1(\Omega)} + |u|_{(H^1(\Omega))^d}). \tag{2.34}$$

Proof. We start with

$$\|p^I - p_h\|_{Q_h} \le \|p^I - p^{I_w}\|_{Q_h} + \|p^{I_w} - p_h\|_{Q_h}.$$

The second term is bounded by Theorem 2.6. For the first term, we use the Bramble–Hilbert Lemma [11] and that the operator $(\cdot)^{I_w}$ is exact for constants. Letting $\bar{p}_E = \frac{1}{|E|}\int_E p \ \mathrm{d}V$, we have

$$\begin{aligned}\|p^I - p^{I_w}\|_{Q_h} &= \left(\sum_E \frac{1}{|E|} \left(\int_E w_E(\bar{p}_E - p) \, \mathrm{d}V \right)^2 \right)^{1/2} \le \left(\sum_E \frac{1}{|E|} \left(\|w_E\|_{L^\infty(E)} \int_E |(\bar{p}_E - p)| \, \mathrm{d}V \right)^2 \right)^{1/2} \\ &\le w_E^{\max} \|\bar{p} - p\|_{L^2(\Omega)} \le Ch|p|_{H^1(\Omega)}.\end{aligned}$$

Combining the above bounds implies the statement of the corollary. □

2.4. Superconvergence of pressure

In this section we prove second-order convergence for $\|p_h - p^{I_w}\|_{Q_h}$. Note that $\|p_h - p^I\|_{Q_h}$ is not in general superconvergent, *i.e.*, there may not be second-order convergence at the centroids of the elements. This is confirmed by numerical experiments in Section 5.

We require the existence of two lifting operators $R_E, \tilde{R}_E : X_h(E) \to H(E;\mathrm{div})$ defined locally over each element and satisfying the following properties:

$$R_E(v_0^I) = v_0, \text{ for all constant vectors } v_0, \tag{2.35}$$

$$\nabla \cdot R_E(v_E) = \mathcal{DIV}\, v_E \text{ in } E, \tag{2.36}$$

$$\nabla \cdot \tilde{R}_E(v_E) = w_E \mathcal{DIV}\, v_E \text{ in } E, \tag{2.37}$$

$$R_E(v_E) \cdot n_E^e = v_E^e \text{ on } e \subset \partial E, \tag{2.38}$$

$$\tilde{R}_E(v_E) \cdot n_E^e = w_e v_E^e \text{ on } e \subset \partial E, \tag{2.39}$$

$$\|R_E(v_E)\|_{(L^2(E))^d} \le C\|v_E\|_{X_{h,E}}, \tag{2.40}$$

$$\|\tilde{R}_E(v_E)\|_{(L^2(E))^d} \le C\|v_E\|_{X_{h,E}}. \tag{2.41}$$

Lemma 2.8. *The lifting operators R_E and $\tilde{R}_E$ define a bilinear form,*

$$[u_E, v_E]_E = \int_E \bar{K}_E^{-1} R_E(u_E) \cdot \tilde{R}_E(v_E) \tag{2.42}$$

that satisfies condition ($\widetilde{S2}$).

Proof. We can demonstrate the result by observing that for all linear q^1 and all $v_E \in X_h(E)$,

$$\begin{aligned}
[(\bar{K}_E \nabla q^1)^I, v_E]_E &= \int_E \bar{K}_E^{-1} R_E((\bar{K}_E \nabla q^1)^I) \cdot \tilde{R}_E(v_E)\, \mathrm{d}V \\
&= \int_E \bar{K}_E^{-1} \bar{K}_E \nabla q^1 \cdot \tilde{R}_E(v_E)\, \mathrm{d}V \ \text{(using (2.35))} \\
&= \sum_{e \in \partial E} \int_e q^1 \tilde{R}_E(v_E) \cdot n_E^e \, \mathrm{d}S - \int_E q^1 \nabla \cdot \tilde{R}_E(v_E)\, \mathrm{d}V \\
&= \sum_{e \in \partial E} v_E^e \int_e w_e q^1 \, \mathrm{d}S - \int_E w_E q^1 \mathcal{DIV}\, v_E \, \mathrm{d}V \ \text{(using (2.39) and (2.37))}.
\end{aligned} \tag{2.43}$$

□

We assume that the choice of bilinear form (2.42) satisfies property ($S1$). In Section 2.4.1 we present a construction of the lifting operators on rectangles that satisfies ($S1$). A discussion on the verification of ($S1$) in the general case is given in Section 3.

The lifting operators R_E and $\tilde{R}_E$ can be used to show that our MFD method is equivalent to a Petrov–Galerkin MFE method. Let

$$\mathbf{V}_h = \{\mathbf{v} \in H(\Omega;\mathrm{div}) : \forall E \in \mathcal{T}_h,\ \mathbf{v}|_E = R_E(v_h|_E),\ v_h \in X_h\},$$

$$\tilde{\mathbf{V}}_h = \{\mathbf{v} \in H(\Omega;\mathrm{div}) : \forall E \in \mathcal{T}_h,\ \mathbf{v}|_E = \tilde{R}_E(v_h|_E),\ v_h \in X_h\}.$$

Note that, due to (2.38) and (2.39), vectors in $\mathbf{V}_h$ and $\tilde{\mathbf{V}}_h$ have continuous normal components across faces, therefore both spaces are subspaces of $H(\Omega;\mathrm{div})$. For the scalar space, define $W_h \subset L^2(\Omega)$ with $W_h|E = P_0(E)$.

Proposition 2.9. *The MFD method (2.17)–(2.18) with velocity bilinear form defined by (2.42) is equivalent to the Petrov–Galerkin MFE method:*

$$\text{Find } \mathbf{u}_h \in \mathbf{V}_h \text{ and } p_h \in W_h \text{ such that,}$$

$$\int_\Omega \bar{K}^{-1}\mathbf{u}_h \cdot \mathbf{v}_h \, \mathrm{d}V - \int_\Omega p_h \nabla \cdot \mathbf{v}_h \, \mathrm{d}V = 0 \qquad \forall \mathbf{v}_h \in \tilde{\mathbf{V}}_h \tag{2.44}$$

$$\int_\Omega \nabla \cdot \mathbf{u}_h q_h \, \mathrm{d}V = \int_\Omega f q_h \, \mathrm{d}V \qquad \forall q \in W_h. \tag{2.45}$$

Proof. The equivalence of the velocity bilinear forms in (2.17) and (2.44) follows immediately from (2.42). The equivalence of the divergence bilinear forms in (2.17) and (2.44) follows from (2.37) and the property (2.14) of w_E. Similarly, the equivalence of (2.18) and (2.45) follows from (2.36). □

Remark 2.10. The test velocity test space $\tilde{\mathbf{V}}_h$ is based on a non-zero modification of $\mathbf{V}_h$ on the boundaries of the elements. Such a space is typically avoided in classical finite element implementations, as it makes the task of maintaining conformity (in this case, continuity of the normal component) more difficult. However, this presents very little difficulty in the setting of the MFD method, as we do not require construction of the vector space on the interior, nor do we need to preform a quadrature in order to construct the stiffness matrix. In fact we do not need to explicitly compute the weighting functions on the faces (w_e). All that is required is to make a single choice of point x_e for each face, and make sure to consistently use the same point when calculating the local matrices over all the cells in the domain.

We will need the following result proved in Lemma 3.3 in [41]:

Lemma 2.11. *For any $v \in (H^1(E))^d$, let v_0 be the mean value of v on E. Then, there exists a constant C independent of h such that*

$$\|v^I - v_0^I\|_{X_{h,E}} \leq C h_E |v|_{(H^1(E))^d}. \tag{2.46}$$

For the rest of this subsection we assume that $w_E \in H^1(E)$ and $w_e \in H^1(e)$. In fact, one can construct affine weighting functions satisfying (2.14) and (2.15), respectively. It is easy to check that $\|w_E\|_{H^1(E)}$ and $\|w_e\|_{H^1(e)}$ are independent of h_E and h_e.

The lifting operator $\tilde{R}_E$ does not in general map constants to constants (as in (2.35)). However, we associate $\tilde{R}_E$ with a tensor T_E with the property that for a constant vector v_0,

$$\tilde{R}_E(v_0^I) = T_E v_0. \tag{2.47}$$

We require that the operator T_E be bounded:

$$\|T_E v_0\|_{(L^2(E))^d} + \|\nabla \cdot T_E v_0\|_{L^2(E)} + \|\operatorname{curl} T_E v_0\|_{L^2(E)} \leq C \|v_0\|_{(L^2(E))^d}. \tag{2.48}$$

To justify the above assumption, we observe that in fact $\nabla \cdot T_E v_0 = 0$ due to (2.37). In addition, we have the freedom of fixing $\operatorname{curl} \tilde{R}_E(v_E)$ in a way that $\operatorname{curl} T_E v_0 = 0$ or at least $\|\operatorname{curl} T_E v_0\|_{L^2(E)} \leq C \|v_0\|_{(L^2(E))^d}$ for any constant vector v_0, where C depends on $|w_E|_{H^1(E)}$ Note that fixing $\operatorname{curl} \tilde{R}_E(v_E)$ makes the definition of $\tilde{R}_E(v_E)$ unique and the space to which it belongs finite dimensional. We further note that (2.39) implies that for a constant vector v_0,

$$T_E v_0 \cdot n_E^e = w_e v_0 \cdot n_E^e \text{ on } e \subset \partial E,$$

which, due to (2.15) and the Friedrichs inequality [11], implies that

$$\|(T_E v_0 - v_0) \cdot n_E^e\|_{L^2(e)} \leq C h_E \|v_0 \cdot n_E^e\|_{L^2(e)}, \tag{2.49}$$

where C depends on $|w_e|_{H^1(e)}$. We next utilize the decomposition $T_E v_0 - v_0 = \nabla\varphi + \operatorname{curl}\psi$, where, in $\mathbb{R}^2$, $\varphi \in H^1(E)\setminus\mathbb{R}$ is the unique solution to

$$\Delta\varphi = \nabla\cdot(T_E v_0 - v_0) \text{ in } E, \quad \nabla\varphi\cdot n_E = (T_E v_0 - v_0)\cdot n_E \text{ on } \partial E,$$

and $\psi \in H^1(E)$ is the unique solution to

$$\Delta\psi = \operatorname{curl}(T_E v_0 - v_0) \text{ in } E, \quad \psi = 0 \text{ on } \partial E,$$

with a similar representation in $\mathbb{R}^3$, see [31]. Elliptic regularity and a scaling argument imply that

$$\|T_E v_0 - v_0\|_{(L^2(E))^d} \le C(h_E^{1/2}\|(T_E v_0 - v_0)\cdot n_E\|_{L^2(\partial E)} + h_E\|\nabla\cdot(T_E v_0 - v_0)\|_{L^2(E)} + h_E\|\operatorname{curl}(T_E v_0 - v_0)\|_{L^2(E)}),$$

which, combined with (2.49), (2.48), and the trace inequality $h_E^{1/2}\|v_0\cdot n_E\|_{L^2(\partial E)} \le C\|v_0\|_{(L^2(E))^d}$, implies that

$$\|T_E v_0 - v_0\|_{(L^2(E))^d} \le C h_E \|v_0\|_{(L^2(E))^d}. \tag{2.50}$$

We have the following results.

Lemma 2.12. *Assume that an operator T_E with properties (2.47) and (2.48) exists. Then, for all $v \in (H^1(E))^d$,*

$$\|R_E(v^I) - v\|_{(L^2(E))^d} \le C h_E |v|_{(H^1(E))^d}, \tag{2.51}$$

$$\|\tilde{R}_E(v^I) - v\|_{(L^2(E))^d} \le C h_E \|v\|_{(H^1(E))^d}. \tag{2.52}$$

Proof. Let v_0 be the $L^2(E)$ projection of v. Using (2.35), (2.40) and (2.46), we have

$$\|R_E(v^I) - v\|_{(L^2(E))^d} \le \|R_E(v^I - v_0^I)\|_{(L^2(E))^d} + \|v_0 - v\|_{(L^2(E))^d} \le C h_E |v|_{(H^1(E))^d},$$

where we also used that

$$\|v - v_0\|_{(L^2(E))^d} \le C h_E |v|_{(H^1(E))^d}. \tag{2.53}$$

Similarly, using (2.41), (2.46), (2.47), (2.50) and (2.53),

$$\|\tilde{R}_E(v^I) - v\|_{(L^2(E))^d} \le \|\tilde{R}_E(v^I - v_0^I)\|_{(L^2(E))^d} + \|T_E v_0 - v_0\|_{(L^2(E))^d} + \|v_0 - v\|_{(L^2(E))^d} \le C h_E \|v\|_{(H^1(E))^d}. \quad \square$$

Theorem 2.13. *Assume the existence of lifting operators R_E and $\tilde{R}_E$ with properties (2.35)–(2.41) and the choice of velocity bilinear form (2.42). Assume also that (2.42) satisfies (S1) and that Ω is convex. Then the solution p_h to (2.17)–(2.18) satisfies*

$$\|p_h - p^{I_w}\|_{Q_h} \le C h^2 (|p|_{H^2(\Omega)} + |p|_{H^1(\Omega)} + \|u\|_{(H^1(\Omega))^d} + |f|_{H^1(\Omega)}). \tag{2.54}$$

Proof. We start by defining φ and ψ such that

$$\varphi = K\nabla\psi, \quad \nabla\cdot\varphi = p_h - p^{I_w} \text{ in } \Omega, \quad \psi = 0 \text{ on } \partial\Omega. \tag{2.55}$$

In the above, by abuse of notation, $p_h - p^{I_w}$ is identified with a piecewise constant function. Let $\varphi_h = \varphi^I$, and note that by (2.9), φ_h satisfies

$$\mathcal{DIV}\,\varphi_h = p_h - p^{I_w}.$$

We require H^2-regularity of problem (2.55). Conditions can be found in [32], which in this case can be satisfied by assuming convexity of Ω and using (2.5). As a result we have,

$$\|\psi\|_{H^2(\Omega)} \le C\|p_h - p^{I_w}\|_{L^2(\Omega)} = C\|p_h - p^{I_w}\|_{Q_h}. \tag{2.56}$$

We have

$$\begin{aligned}
\|p_h - p^{I_w}\|_{Q_h}^2 &= [p_h - p^{I_w}, \mathcal{DIV}\,\varphi_h]_{Q_h} \\
&= [u_h, \varphi_h]_{X_h} - \int_\Omega p\,\nabla\cdot\tilde{R}(\varphi_h)\,\mathrm{d}V \ \text{(using (2.17) and (2.37))} \\
&= [u_h, \varphi_h]_{X_h} + \int_\Omega \nabla p\cdot\tilde{R}(\varphi_h)\,\mathrm{d}V \\
&= \sum_E \left[\int_E \bar{K}_E^{-1}(R_E(u_E) - u)\cdot\tilde{R}_E(\varphi_E)\,\mathrm{d}V + \int_E (\bar{K}_E^{-1} - K^{-1})u\cdot\tilde{R}_E(\varphi_E)\,\mathrm{d}V\right] \\
&= \sum_E \left[\int_E (\bar{K}_E^{-1} - K^{-1})(R_E(u_E) - u)\cdot\tilde{R}_E(\varphi_E)\,\mathrm{d}V\right. \\
&\quad \left. + \int_E K^{-1}(R_E(u_E) - u)\cdot\tilde{R}_E(\varphi_E)\,\mathrm{d}V + \int_E (\bar{K}_E^{-1} - K^{-1})u\cdot\tilde{R}_E(\varphi_E)\,\mathrm{d}V\right] \\
&\equiv J_1 + J_2 + J_3
\end{aligned}$$

For J_1, using (2.7), we have,

$$|J_1| \le Ch\|R(u_h) - u\|_{(L^2(\Omega))^d}\|\tilde{R}(\varphi)\|_{(L^2(\Omega))^d} \le Ch^2(|p|_{H^2(\Omega)} + |p|_{H^1(\Omega)} + |u|_{(H^1(\Omega))^d})\|p_h - p^{I_w}\|_{Q_h},$$

where for the second step we used

$$\begin{aligned}
\|R(u_h) - u\|_{(L^2(E))^d} &\le C\|R(u_h - u^I)\|_{(L^2(\Omega))^d} + \|R(u^I) - u\|_{(L^2(\Omega))^d} \\
&\le C\|u_h - u^I\|_{X_h} + \|R(u^I) - u\|_{(L^2(\Omega))^d} \ \text{(using (2.40))} \\
&\le Ch(|p|_{H^2(\Omega)} + |p|_{H^1(\Omega)} + |u|_{(H^1(\Omega))^d}) \ \text{(by Thm. 2.4 and (2.51))},
\end{aligned} \tag{2.57}$$

as well as, using (2.41), (2.20), (2.5), and (2.56),

$$\|\tilde{R}(\varphi_h)\|_{(L^2(\Omega))^d} \le C\|\varphi_h\|_{X_h} \le C\|\varphi\|_{(H^1(\Omega))^d} \le C\|\psi\|_{H^2(\Omega)} \le C\|p_h - p^{I_w}\|_{Q_h}. \tag{2.58}$$

For J_2, we start by adding and subtracting φ,

$$J_2 = \int_\Omega K^{-1}(R(u_h) - u)\cdot(\tilde{R}(\varphi_h) - \varphi)\,\mathrm{d}V + \int_\Omega K^{-1}(R(u_h) - u)\cdot\varphi\,\mathrm{d}V \equiv J_{21} + J_{22}.$$

For J_{21}, using (2.52) and (2.57), we have

$$|J_{21}| \le Ch^2(|p|_{H^2(\Omega)} + |p|_{H^1(\Omega)} + |u|_{(H^1(\Omega))^d})\|p_h - p^{I_w}\|_{Q_h}.$$

We can bound J_{22} by noting that,

$$J_{22} = \int_\Omega (R(u_h) - u)\cdot\nabla\psi\,\mathrm{d}V = -\int_\Omega \nabla\cdot(R(u_h) - u)\psi\,\mathrm{d}V = \int_\Omega (f^I - f)(\psi - \psi^I)\,\mathrm{d}V,$$

which, combined with the Bramble–Hilbert Lemma, implies that

$$|J_{22}| \le Ch^2|f|_{H^1(\Omega)}\|p_h - p^{I_w}\|_{Q_h}.$$

For J_3, we add and subtract φ, obtaining

$$J_3 = \sum_E \int_E \left[(\bar{K}_E^{-1} - K^{-1})u\cdot(\tilde{R}_E(\varphi_E) - \varphi)\,\mathrm{d}V + \int_E (\bar{K}_E^{-1} - K^{-1})u\cdot\varphi\,\mathrm{d}V\right] \equiv J_{31} + J_{32}.$$

Using (2.7) and (2.52) and an argument similar to (2.58), J_{31} is bounded by,

$$|J_{31}| \leq Ch^2 \|u\|_{(L^2(\Omega))^d} \|p_h - p^{I_w}\|_{Q_h}.$$

For expression J_{32}, we have,

$$\begin{aligned} J_{32} &= \sum_E \int_E (\bar{K}_E^{-1} - K^{-1}) u \cdot K \nabla \psi \, \mathrm{d}V = \sum_E \int_E (K - \bar{K}_E) \bar{K}_E^{-1} u \cdot K^{-1} K \nabla \psi \, \mathrm{d}V \\ &= \sum_E \int_E (K - \bar{K}_E) \bar{K}_E^{-1} (u - u_0) \cdot \nabla \psi \, \mathrm{d}V + \int_E (K - \bar{K}_E) \bar{K}_E^{-1} u_0 \cdot (\nabla \psi - (\nabla \psi)_0) \, \mathrm{d}V. \end{aligned}$$

An application of (2.6) and the Bramble–Hilbert Lemma gives

$$|J_{32}| \leq Ch^2 \|u\|_{(H^1(\Omega))^d} \|p_h - p^{I_w}\|_{Q_h}.$$

Combining all bounds gives the desired result. □

Remark 2.14. An alternative approach to pressure superconvergence is to use a velocity bilinear form that is an approximate quadrature rule for the integral of the product of the lifting operators. In this case, we restrict $[\cdot,\cdot]_E$ to a symmetric form. Let

$$\sigma_E(K^{-1}; u_E, v_E) = [u_E, v_E]_E - \int_E K^{-1} R_E(u_E) \cdot \tilde{R}_E(v_E) \, \mathrm{d}V. \tag{2.59}$$

The proof of the result below follows the exposition found in ([41], Thm. 3.3).

Theorem 2.15. *Assume the existence of lifting operators R_E and $\tilde{R}_E$ with properties (2.35)–(2.41) and that the choice of a symmetric velocity bilinear form $[\cdot,\cdot]_E$ satisfies for all $u, v \in (H^1(E))^d$*

$$|\sigma_E(K^{-1}; (u^I)_E, (v^I)_E)| \leq Ch_E^2 \|u\|_{(H^1(E))^d} \|v\|_{(H^1(E))^d}. \tag{2.60}$$

Then the solution p_h to problem (2.17)–(2.18) satisfies

$$\|p_h - p^{I_w}\|_{Q_h} \leq Ch^2 (|p|_{H^2(\Omega)} + |p|_{H^1(\Omega)} + \|u\|_{(H^1(\Omega))^d} + |f|_{H^1(\Omega)}).$$

Remark 2.16. The superconvergence result $\|p_h - p^{I_w}\|_{Q_h} \leq Ch^2$ can be explored to reconstruct a second-order accurate piecewise linear approximation of the pressure. For example, following the approach in [17], one can consider on each element E the linear function

$$p_E^R(x) = p_E + \nabla_E p_E \cdot (x - x_E),$$

where $\nabla_E p_E$ is a discrete gradient based on a constant velocity reconstruction. We note that $p_E^R(x_E) = p_E$, *i.e.*, the linear reconstruction matches the computed constant pressure at the shifted superconvergent point x_E. A detailed analysis of the post-processing is beyond the scope of the paper and it will be investigated in the future.

2.4.1. Lifting operators for a square element

We present an example of lifting operators R_E and $\tilde{R}_E$ satisfying (2.35)–(2.41) over a square reference element $E = [0,1]^2$, see Figure 1 (*left*), where $x_E = (\tilde{x}, \tilde{y})^T$, $x_{e_2} = x_{e_4} = \tilde{x}$, $x_{e_1} = x_{e_3} = \tilde{y}$. For operator R_E, we use the standard lowest order Raviart–Thomas (RT_0) interpolant:

$$R_E(v_E) = \begin{pmatrix} v_3 + (v_1 - v_3)x \\ v_4 + (v_2 - v_4)y \end{pmatrix},$$

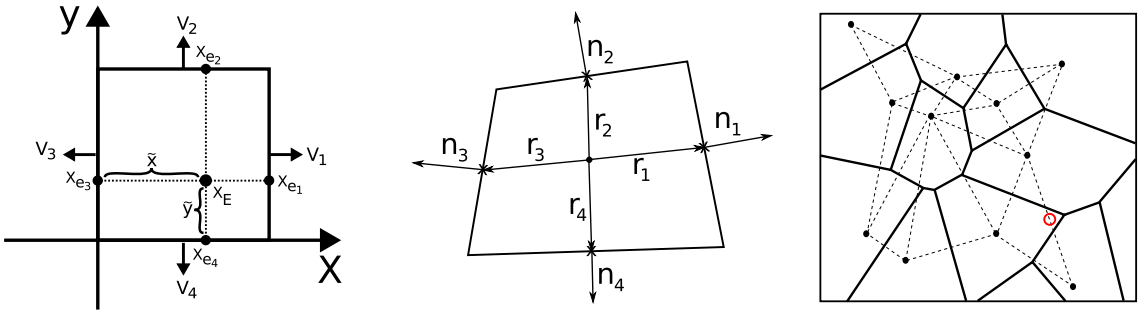

FIGURE 1. *Right*: The reference element for the lifting operator $\tilde{R}$. *Center*: Vectors r_i and n_i used in the definition of matrices $\mathbf{R}_E$ and $\mathbf{N}_E$. *Right*: A two-dimensional Voronoi diagram (*solid line*) and the lines joining adjacent Voronoi generating points (*dashed line*).

where $v_i = v_E^{e_i}$. It is well-known [12] that the RT_0 interpolant satisfies (2.35), (2.36) and (2.40). The lifting operator $\tilde{R}_E$ is defined as

$$\tilde{R}_E(v_E) = \begin{pmatrix} (v_3 + (v_1 - v_3)W_x(x))w_y(y) \\ (v_4 + (v_2 - v_4)W_y(y))w_x(x) \end{pmatrix},$$

with

$$W_x(0) = 0, \quad W_x(1) = 1, \quad \frac{\partial}{\partial x} W_x = w_x, \tag{2.61}$$

and similarly for W_y, where $w_x(x)$ and $w_y(y)$ are the weighting functions on the horizontal and vertical faces, respectively. The lifting operator $\tilde{R}_E$ directly satisfies conditions (2.37) and (2.39), with the corresponding volume weighting $w_E(x, y) = w_x(x)w_y(y)$. We can construct functions of the form $W_x(x) = \frac{a}{2}x^2 + bx$, and $w_x(x) = ax + b$. One can verify that the choice $a = -6 + 12\tilde{x}, b = 4 - 6\tilde{x}$, results in functions that satisfy (2.15) and (2.61). It is easy to check that (2.41) holds and that (2.47) and (2.48) hold with

$$T_E = \begin{pmatrix} w_y & 0 \\ 0 & w_x \end{pmatrix}.$$

Lemma 2.17. *The matrix M_E formed by the bilinear form (2.42) satisfies condition (S1).*

Proof. Consider an element $E = (0, h_x) \times (0, h_y)$. The result can be observed directly by first formulating M_E in terms of $\tilde{x}, \tilde{y}$ and the width of the element h_x, h_y, giving

$$M_E = \frac{1}{12} \begin{pmatrix} h_y(7h_x - 6\tilde{x}) & 0 & -h_y(h_x - 6\tilde{x}) & 0 \\ 0 & h_x(7h_y - 6\tilde{y}) & 0 & -h_x(h_y - 6\tilde{y}) \\ h_y(5h_x - 6\tilde{x}) & 0 & h_y(h_x + 6\tilde{x}) & 0 \\ 0 & h_x(5h_y - 6\tilde{y}) & 0 & h_x(h_y + 6\tilde{y}). \end{pmatrix}.$$

A direct calculation produces two distinct double eigenvalues $\{\frac{1}{6}h_xh_y, \frac{1}{2}h_xh_y\}$, which implies that M_E satisfies (2.11). The eigenvalues of $M_E^T M_E$ are dependent on the choice of $\tilde{x}$ and $\tilde{y}$. The maximum eigenvalue attained over the ranges $\tilde{x} \in (0, h_x)$ and $\tilde{y} \in (0, h_y)$ is $\frac{19+5\sqrt{13}}{72}(h_xh_y)^2$, which guarantees (2.12). □

We have shown that the lifting operators satisfy all conditions needed for the pressure superconvergence in Theorem 2.13 with velocity inner product defined by (2.42). For the alternative approach to pressure superconvergence with quadrature found in Theorem 2.15, consider the case of diagonal permeability with

$$\bar{K}_E = \begin{pmatrix} k_x & 0 \\ 0 & k_y \end{pmatrix}.$$

We can define the velocity inner product *via* (2.10) with a diagonal quadrature matrix $\mathbf{M}_E$:

$$\mathbf{M}_E^{(1,1)} = \frac{1-\tilde{x}}{k_x}, \quad \mathbf{M}_E^{(2,2)} = \frac{1-\tilde{y}}{k_y}, \quad \mathbf{M}_E^{(3,3)} = \frac{\tilde{x}}{k_x}, \quad \mathbf{M}_E^{(4,4)} = \frac{\tilde{y}}{k_y}. \tag{2.62}$$

Note that the positivity of the entries ensures satisfaction of condition $(S1)$ and that condition $(\widetilde{S2})$ is satisfied by the above choice of inner product. The choice of quadrature (2.62) satisfies condition (2.60) and the proof is shown in Appendix A.

3. Matrix construction

We have explicitly defined the $\mathcal{DIV}$ operator, as well as the pressure inner product $[\cdot,\cdot]_{Q_h}$. What remains is to define, for the general case, the velocity bilinear form $[\cdot,\cdot]_E$. The discretization yields a convergent solution if the inner product satisfies the stability $(S1)$ and consistency $(\widetilde{S2})$ conditions. The second condition is the main focus of constructing the appropriate inner product.

Define matrices $\mathbf{R}_E \in \mathbb{R}^{k_E \times d}$ and $\mathbf{N}_E \in \mathbb{R}^{k_E \times d}$ as

$$\mathbf{R}_E = \begin{pmatrix} |e_1|(x_{e_1} - x_E)^T \\ \vdots \\ |e_{k_E}|(x_{e_{k_E}} - x_E)^T \end{pmatrix}, \quad \mathbf{N}_E = \begin{pmatrix} (\bar{K}_E\, n_{e_1})^T \\ \vdots \\ (\bar{K}_E\, n_{e_{k_E}})^T \end{pmatrix}, \tag{3.1}$$

see Figure 1 (*center*). Condition $(\widetilde{S2})$ can be guaranteed with $\mathbf{M}_E$ defined to satisfy

$$\mathbf{M}_E\mathbf{N}_E = \mathbf{R}_E. \tag{3.2}$$

Note that by setting $w_E = 1$ and $w_e = 1$ we retrieve the original definition of the MFD method [15], in which case, x_E corresponds to the centroid of element E, and x_e would correspond to the centroid of face e. Also note that we do not require explicit construction of the weighting functions in order to build the linear system.

The authors of [15] demonstrate how to construct $\mathbf{M}_E$ to satisfy (3.2). This is done by first defining $\mathbf{C}_E \in \mathbb{R}^{k_E \times k_E - d}$ such that $\mathbf{N}_E^T\mathbf{C}_E = 0$. It is shown in [15] that without boundary weights,

$$\mathbf{R}_E^T\mathbf{N}_E = |E|\bar{K}_E. \tag{3.3}$$

As a result, $\mathbf{M}_E$ defined as

$$\mathbf{M}_E = \frac{1}{|E|}\mathbf{R}_E\bar{K}_E^{-1}\mathbf{R}_E^T + \mathbf{C}_E\mathbf{U}_E\mathbf{C}_E^T, \tag{3.4}$$

for a positive-definite $\mathbf{U}_E \in \mathbb{R}^{(K_E-d)\times(K_E-d)}$ satisfies (3.2). Due to the modification $(\widetilde{S2})$ of condition (S2), equality (3.3) no longer holds. However, we can still proceed by using the form proposed by [43],

$$\mathbf{M}_E = \mathbf{R}_E(\mathbf{R}_E^T\mathbf{N}_E)^{-1}\mathbf{R}_E^T + \mathbf{C}_E\mathbf{U}_E\mathbf{C}_E^T.$$

We note that $\mathbf{R}_E^T\mathbf{N}_E$ may not always be invertible, although this occurs very rarely in practice. Singularity can be detected numerically by the direct solver, in which case one can use an alternative form found in [41],

$$\mathbf{M}_E = \mathbf{R}_E(\mathbf{N}_E^T\mathbf{N}_E)^{-1}\mathbf{N}_E^T + \mathbf{C}_E\mathbf{U}_E\mathbf{C}_E^T.$$

The matrix $\mathbf{N}_E^T\mathbf{N}_E$ is guaranteed to be invertible, since the shape regularity of the elements and the the fact that K is symmetric and positive definite imply that $\mathbf{N}_E$ has full rank.

Remark 3.1. As we pointed above, $\mathbf{R}_E^T\mathbf{N}_E$ reduces to $|E|\bar{K}_E$ in the case when no boundary points are shifted, resulting in a symmetric $\mathbf{M}_E$. Keeping the boundary points set to the centroids of the faces corresponds to the Hybrid Mimetic Mixed (HMM) method [23], which is also related to the more recent development of gradient schemes [24]. Therefore our method can be viewed as an extension to the framework of gradient schemes.

Remark 3.2. The verification of assumption $(S1)$ in the general non-symmetric case is a difficult task and it depends on the shape regularity of the elements and the anisotropy of permeability tensor K. We refer the reader to [37,41] for analysis in the case of MPFA methods. In the next section we show that on general Voronoi meshes and isotropic permeability, a special choice of the element and face points results in a diagonal matrix $\mathbf{M}_E$ that satisfies $(S1)$.

4. Finite volume methods and the MFD method

Finite Volume Methods (FVM) are based on an application of the divergence theorem to each element E in the domain,

$$\int_E \nabla \cdot u \, \mathrm{d}V = \sum_{e\in\partial E} \int_e u \cdot n_E^e \, \mathrm{d}S \approx \frac{1}{|E|} \sum_{e\in\partial E} |e| u_E^e.$$

Finite volume discretizations are distinguished by how the flux (u_E^e) is approximated. In the case of porous media applications, the flux of the fluid is a function of the fluid pressure. Each element in the domain has a single, piecewise constant pressure degree of freedom (p_E), and each face in the mesh has a single flux representing the normal component of the velocity across that face (u_E^e). The flux is then related to the pressure via a function

$$u_E^e = F(p_h).$$

The choice of function F is what distinguishes a particular FV method. When the velocity at face e is approximated using *two* adjacent pressures, we have a two-point flux approximation (TPFA). When more than two pressures are used, the method is referred to as a multi-point flux approximation (MPFA).

The MFD method, much like the related MFE method, produces a saddle-point problem with both velocity and pressure unknowns:

$$\begin{pmatrix} M & -\mathcal{DIV}^* \\ \mathcal{DIV} & 0 \end{pmatrix} \begin{pmatrix} u_h \\ p_h \end{pmatrix} = \begin{pmatrix} 0 \\ f^I \end{pmatrix}.$$

One can observe the relation between FVM and the MFD method by explicitly expressing the velocity unknown as a function of pressure:

$$u_h = -M^{-1}\mathcal{DIV}^* \, p_h = F_{\mathrm{MFD}}(p_h).$$

The nature of the relation between p_h and u_h is a direct consequence of the structure of M^{-1}. In general, the matrix M^{-1} is dense, causing the velocity at every face to be a function of all the pressure unknowns. However, constructing a diagonal matrix M leads trivially to a diagonal M^{-1}. In this case, due to the structure of matrix $\mathcal{DIV}^*$, velocities are a linear function of two pressures, resulting in a TPFA scheme.

There is a simple geometric criterion that indicates when diagonality can be achieved in the MFD method. The global matrix M is formed from the summation of local matrices, $M = \sum_E \mathbf{M}_E$. Matrices $\mathbf{M}_E$ must satisfy the relation (3.2). When the rows of $\mathbf{N}_E$ are collinear to the rows of $\mathbf{R}_E$, a simple scaling of the rows of $\mathbf{N}_E$ satisfies (3.2), *i.e.*, a diagonal matrix $\mathbf{M}_E$ suffices. Therefore, our objective is to construct matrices $\mathbf{R}_E$ with rows collinear to the rows of $\mathbf{N}_E$. The original MFD method sets the point x_E to the centroid of the cells and the points x_e to the centroids of the faces. Our generalization allows the point x_E to be shifted on the interior of the cell, and the points x_e to be shifted on the plane of the faces. By shifting these points, we can establish collinearity of the rows of $\mathbf{R}_E$ and $\mathbf{N}_E$, resulting in a diagonal matrix $\mathbf{M_E}$. This can be achieved for general Voronoi meshes when K is a scalar function. A Voronoi diagram is a tessellation of $\mathbb{R}^d$ relative to a set of points known as generators.

Definition 4.1. Voronoi Diagram. Given a set of generating points, $V = \{V_i \in \mathbb{R}^d\}$, we define the Voronoi tessellation $\mathcal{T}_h = \{E_i\}$ as

$$E_i = \{x \in \mathbb{R}^d \mid d(x, V_i) \leq d(x, V_j)\ \forall j \neq i\}.$$

It is a direct consequence of the definition of Voronoi diagrams that the line joining two adjacent generating points is always perpendicular to the common face between them and bisected by the plane of the face. For two adjacent points, V_i and V_j, with associated face e, we refer to the midpoint between them as b_e.

Lemma 4.2. *For a Voronoi polyhedron with isotropic permeability ($\bar{K}_E = \kappa_E I$), by setting $x_E = V_E$ and $x_e = b_e$, a diagonal matrix $\mathbf{M}_E$ can be constructed that satisfies both conditions $(S1)$ and $(\widetilde{S2})$.*

Proof. Let us denote the rows of $\mathbf{R}_E$ and $\mathbf{N}_E$ by R_e^T and N_e^T, respectively. Since the line joining two adjacent generating points is orthogonal to the Voronoi face between them, the vectors R_e are collinear to N_e. That is,

$$R_e = \frac{|e|\|R_e\|}{\kappa_E} N_e,$$

where $\|\cdot\|$ is the Euclidean norm on $\mathbb{R}^d$. Therefore, a diagonal matrix $\mathbf{M}_E$ with choice of entries $(\mathbf{M}_E)_{ii} = \frac{|e_i|\|R_{e_i}\|}{\kappa_E}$ satisfies (3.2), which implies condition $(\widetilde{S2})$. It is also easy to see that it satisfies condition $(S1)$. □

Note that the point b_e may fall outside of the boundary faces, see the red circle in Figure 1 (*right*). This, however, presents no problems for our definition, as we allow the function w_e to be negative, which can shift the boundary point x_e outside of the face.

5. Numerical results

5.1. Convergence study

In this section we present numerical results for our proposed generalization of the MFD method. The permeability tensor $\bar{K}_E$ is computed at the centroid of each cell E. Given a set of points $z_E \in E$, $\forall E \in \mathcal{T}_h$, define

$$\text{PressErr}(z_E) = \left(\sum_E |E| (p(z_E) - p_E)^2 \right)^{1/2}.$$

Note that

$$\|p^{I_w} - p_h\|_{Q_h} = \left(\sum_E |E| ((p^{I_w})_E - p_E)^2 \right)^{1/2} \approx \left(\sum_E |E| (p(x_E) - p_E)^2 \right)^{1/2} = \text{PressErr}(x_E).$$

Note that for linear $p|_E$, $p_E^{I_w} = p(x_E)$, therefore the above is a second-order approximation. Similarly,

$$\|p^{I} - p_h\|_{Q_h} = \left(\sum_E |E| ((p^{I})_E - p_E)^2 \right)^{1/2} \approx \left(\sum_E |E| (p(C_E) - p_E)^2 \right)^{1/2} = \text{PressErr}(C_E),$$

which is also a second order approximation.

We can establish similar norms for the velocity errors. Given a set of points $z_e \in e$, define

$$\text{VelErr}(z_e) = \left(\sum_E |E| \sum_{e \in \partial E} (u(z_e) \cdot n_E^e - u_E^e)^2 \right)^{1/2}.$$

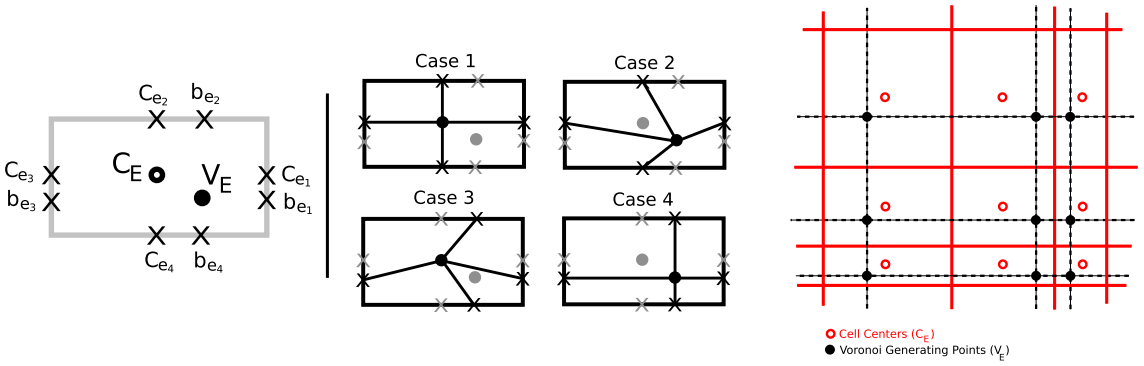

FIGURE 2. *Left and center*: The four test cases based on different locations for points x_e and x_E. *Right*: An illustration of the cell centered points and the Voronoi generating points used for the two-dimensional rectangular grids.

Note that

$$\|u^{I_w} - u_h\|_{X_h} \approx \left(\sum_E |E| \sum_{e \in \partial E} ((u^{I_w})_E^e - u_E^e)^2 \right)^{1/2} \approx \left(\sum_E |E| \sum_{e \in \partial E} ((u(b_e) \cdot n_E^e - u_E^e)^2 \right)^{1/2} = \text{VelErr}(b_e).$$

Note that this is a second order approximation, since for linear $u \cdot n_E^e$ on e, $(u^{I_w})_E^e = u(b_e) \cdot n_E^e$. Similarly,

$$\|u^I - u_h\|_{X_h} \approx \left(\sum_E |E| \sum_{e \in \partial E} ((u^I)_E^e - u_E^e)^2 \right)^{1/2} \approx \left(\sum_E |E| \sum_{e \in \partial E} ((u(c_e) \cdot n_E^e - u_E^e)^2 \right)^{1/2} = \text{VelErr}(c_e).$$

For each mesh, we test four different methods based on choices of points x_E and x_e in $(\widetilde{S2})$:

Case 1: $x_E = C_E, x_e = c_e$, **Case 2:** $x_E = V_E, x_e = c_e$, **Case 3:** $x_E = C_E, x_e = b_e$, **Case 4:** $x_E = V_E, x_e = b_e$.

These four cases are illustrated in Figure 2. In all cases we compute the pressure errors for $z_E = C_E$, the centroid of E, and $z_E = V_E$, the generating point for the Voronoi diagram and the velocity errors for $z_e = c_e$, the centroid of e, and $z_e = b_e$, the Voronoi bisection point.

For Cases 1 and 3, we have

$$\text{PressErr}(C_E) = \text{PressErr}(x_E) \approx \|p^{I_w} - p_h\|_{Q_h} = \|p^I - p_h\|_{Q_h},$$
$$\text{PressErr}(V_E) \text{ is not directly related to either error.}$$

For Cases 2 and 4, we have

$$\text{PressErr}(C_E) \approx \|p^I - p_h\|_{Q_h},$$
$$\text{PressErr}(V_E) = \text{PressErr}(x_E) \approx \|p^{I_w} - p_h\|_{Q_h}.$$

For Cases 1 and 2, we have

$$\text{VelErr}(c_e) = \text{VelErr}(x_e) \approx \|u^{I_w} - u_h\|_{X_h} = \|u^I - u_h\|_{X_h},$$
$$\text{VelErr}(b_e) \text{ is not directly related to either error.}$$

For Cases 3 and 4, we have

$$\text{VelErr}(c_e) \approx \|u^I - u_h\|_{X_h}, \;\; \text{VelErr}(b_e) \approx \|u^{I_w} - u_h\|_{X_h}.$$

The theory predicts for Cases 1 and 3 the following pressure convergence rates:

$$\text{PressErr}(C_E) = O(h^2), \;\; \text{PressErr}(V_E) = O(h).$$

For Cases 2 and 4, we expect the following convergence rates:

$$\text{PressErr}(C_E) = O(h), \;\; \text{PressErr}(V_E) = O(h^2).$$

We expect at least $O(h)$ for all velocity errors. Recall from Section 2.2 that we expect better accuracy for $\|u^{I_w} - u_h\|_{X_h}$ compared to $\|u^I - u_h\|_{X_h}$, which translates to better accuracy for $\text{VelErr}(c_e)$ in Cases 1 and 2 and for $\text{VelErr}(b_e)$ in Cases 3 and 4.

In 2D we consider the following solution and permeability tensor from [15] over the unit square domain $\Omega = (0,1)^2$,

$$p(x,y) = x^3y^2 + x\sin(2\pi xy)\sin(2\pi y), \quad K = \begin{pmatrix} (x+1)^2 + y^2 & -xy \\ -xy & (x+1)^2 \end{pmatrix}.$$

In three dimensions, we use solve a problem over the unit cube $\Omega = (0,1)^3$ with

$$p(x,y,z) = x^3y^2z + x\sin(2\pi xy)\sin(2\pi yz)\sin(2\pi z), \quad K = \begin{pmatrix} 1+y^2+z^2 & -xy & -xz \\ -xy & 1+x^2+z^2 & -yz \\ -xz & -yz & 1+x^2+y^2 \end{pmatrix}.$$

The matrix U_E for all cases is chosen to be $U_E = \frac{|E|}{\text{trace}(K_E)}\mathbb{I}$.

We construct two kinds of meshes, rectangular grids and random Voronoi meshes. The rectangular grids are generated by perturbing evenly spaced points with spacing h by

$$\xi_i = ih + \frac{3}{50}|\sin(4\pi ih)|, \;\; \xi = x, y, z.$$

These points serve as the shifted location V_E for point x_E. The mesh is then constructed as a Voronoi diagram using these points as generating points, see Figure 2 (*right*). This is equivalent to constructing a rectangular mesh in a point-centered fashion, where faces are placed midway between two adjacent points. The centroids of the cells formed by this procedure are the points C_E, see Figure 2 (*right*). The second kind of mesh, the random Voronoi diagrams, are constructed by selecting uniformly distributed random points in the domain as generating points. The mesh is refined by selecting a larger number of randomly generated points unrelated to the previous mesh. Examples of the meshes used can be seen in Figure 3.

The convergence results for Cases 1–4 on rectangular and Voronoi meshes in both two and three dimensions can be seen in Tables 1–4. As predicted by the theory, in all cases we achieve at least first-order convergence for both the pressure and flux variables.

Regarding superconvergence, as predicted, we observe $O(h^2)$ convergence for the pressure at the points x_E, *i.e.*, at points C_E for Cases 1 and 3, and at points V_E for Cases 2 and 4. We observe a reduced convergence rate at the points that are not used in the construction of matrix $\mathbf{M}_E$. We observe velocity superconvergence of at least $O(h^{3/2})$ on rectangular grids in both two and three dimensions. As expected, the convergence is somewhat better at the points x_e, *i.e.* at points c_e for Cases 1 and 2, and points b_e for Cases 3 and 4.

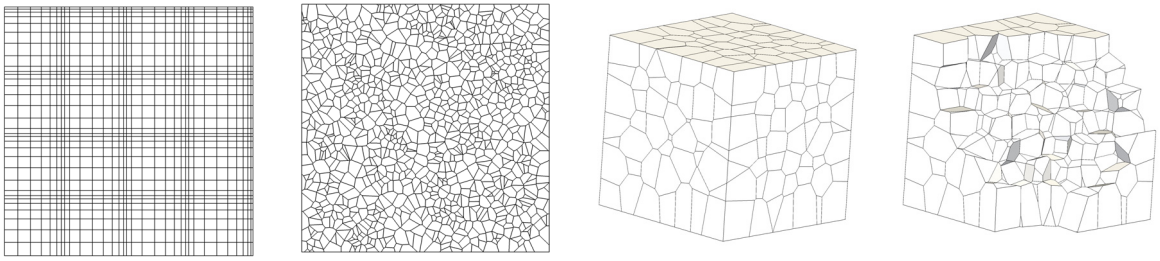

FIGURE 3. The meshes used for the convergence study in two and three dimensions. The plot on the right is a slice of the mesh showing the inner structure of the Voronoi diagram.

TABLE 1. Convergence rates on rectangular grids in two dimensions.

(Case 1: $x_E = C_E$, $x_e = c_e$)								
n	PressErr(C_E)	Conv.	PressErr(V_E)	Conv.	VelErr(c_e)	Conv.	VelErr(b_e)	Conv.
32	3.217e-03	–	8.850e-03	–	2.068e-01	–	2.413e-01	–
64	8.616e-04	1.90	2.766e-03	1.68	6.191e-02	1.74	7.524e-02	1.68
128	2.214e-04	1.96	8.903e-04	1.64	1.753e-02	1.82	2.297e-02	1.71
256	5.607e-05	1.98	2.968e-04	1.58	4.829e-03	1.86	7.088e-03	1.70
(Case 2: $x_E = V_E$, $x_e = c_e$)								
n	PressErr(C_E)	Conv.	PressErr(V_E)	Conv.	VelErr(c_e)	Conv.	VelErr(b_e)	Conv.
32	7.948e-03	–	3.638e-03	–	2.728e-01	–	3.029e-01	–
64	2.558e-03	1.64	9.376e-04	1.96	7.654e-02	1.83	8.526e-02	1.83
128	8.480e-04	1.59	2.371e-04	1.98	2.110e-02	1.86	2.398e-02	1.83
256	2.887e-04	1.55	5.949e-05	1.99	5.849e-03	1.85	6.911e-03	1.80
(Case 3: $x_E = C_E$, $x_e = b_e$)								
n	PressErr(C_E)	Conv.	PressErr(V_E)	Conv.	VelErr(c_e)	Conv.	VelErr(b_e)	Conv.
32	4.154e-03	–	9.510e-03	–	3.177e-01	–	2.754e-01	–
64	1.134e-03	1.87	2.931e-03	1.70	9.395e-02	1.76	8.025e-02	1.78
128	2.929e-04	1.95	9.253e-04	1.66	2.719e-02	1.79	2.258e-02	1.83
256	7.427e-05	1.98	3.037e-04	1.61	8.007e-03	1.76	6.335e-03	1.83
(Case 4: $x_E = V_E$, $x_e = b_e$)								
n	PressErr(C_E)	Conv.	PressErr(V_E)	Conv.	VelErr(c_e)	Conv.	VelErr(b_e)	Conv.
32	7.501e-03	–	3.184e-03	–	2.844e-01	–	2.436e-01	–
64	2.438e-03	1.62	7.901e-04	2.01	8.754e-02	1.70	7.079e-02	1.78
128	8.230e-04	1.57	1.960e-04	2.01	2.716e-02	1.69	2.070e-02	1.77
256	2.840e-04	1.54	4.877e-05	2.01	8.694e-03	1.64	6.237e-03	1.73

5.2. Improved flux approximations

The main objective in this work has been to reduce the MFD method to a TPFA scheme for general Voronoi meshes. As a by-product, our generalization extends the MFD method into a family of non-symmetric Petrov–Galerkin type methods. In this example, we demonstrate the benefits of this additional flexibility.

Consider the domain $\Omega = (0,1)^2$ discretized on a 10×10 mesh with high permeability blocks on the diagonal. Dirichlet boundary condition is set on the bottom left and top right faces of the domain, and no-flux is imposed on the rest of the boundary, see Figure 4a. We test three different positions for the face points x_e in the high permeability cells, see Figure 4b. Case A shifts the points away from the diagonal, Case B keeps the points at the centroid (the original MFD method), and Case C shifts the points toward the diagonal. The three methods are

TABLE 2. Convergence rates on random Voronoi grids in two dimensions.

(Case 1: $x_E = C_E$, $x_e = c_e$)								
n	PressErr(C_E)	Conv.	PressErr(V_E)	Conv.	VelErr(c_e)	Conv.	VelErr(b_e)	Conv.
32	4.394e-03	–	1.653e-02	–	1.043e+00	–	1.233e+00	–
64	1.241e-03	1.82	8.758e-03	0.92	5.100e-01	1.03	5.978e-01	1.04
128	2.857e-04	2.12	4.234e-03	1.05	2.439e-01	1.06	2.860e-01	1.06
256	7.639e-05	1.90	2.126e-03	0.99	1.213e-01	1.01	1.413e-01	1.02
(Case 2: $x_E = V_E$, $x_e = c_e$)								
n	PressErr(C_E)	Conv.	PressErr(V_E)	Conv.	VelErr(c_e)	Conv.	VelErr(b_e)	Conv.
32	1.687e-02	–	6.539e-03	–	1.188e+00	–	1.334e+00	–
64	8.947e-03	0.91	2.080e-03	1.65	5.098e-01	1.22	5.880e-01	1.18
128	4.249e-03	1.07	4.299e-04	2.27	2.359e-01	1.11	2.742e-01	1.10
256	2.129e-03	1.00	1.285e-04	1.74	1.164e-01	1.02	1.345e-01	1.03
(Case 3: $x_E = C_E$, $x_e = b_e$)								
n	PressErr(C_E)	Conv.	PressErr(V_E)	Conv.	VelErr(c_e)	Conv.	VelErr(b_e)	Conv.
32	5.317e-03	–	1.710e-02	–	1.292e+00	–	1.136e+00	–
64	1.452e-03	1.87	8.783e-03	0.96	6.384e-01	1.02	5.565e-01	1.03
128	3.960e-04	1.87	4.248e-03	1.05	2.947e-01	1.12	2.596e-01	1.10
256	1.043e-04	1.92	2.128e-03	1.00	1.473e-01	1.00	1.288e-01	1.01
(Case 4: $x_E = V_E$, $x_e = b_e$)								
n	PressErr(C_E)	Conv.	PressErr(V_E)	Conv.	VelErr(c_e)	Conv.	VelErr(b_e)	Conv.
32	1.646e-02	–	5.631e-03	–	1.379e+00	–	1.202e+00	–
64	8.822e-03	0.90	1.587e-03	1.83	5.995e-01	1.20	5.052e-01	1.25
128	4.240e-03	1.06	3.695e-04	2.10	2.804e-01	1.10	2.365e-01	1.09
256	2.127e-03	1.00	9.556e-05	1.95	1.396e-01	1.01	1.172e-01	1.01

TABLE 3. Convergence rates on rectangular grids in three-dimensions.

(Case 1: $x_E = C_E$, $x_e = c_e$)								
n	PressErr(C_E)	Conv.	PressErr(V_E)	Conv.	VelErr(c_e)	Conv.	VelErr(b_e)	Conv.
8	3.193e-02	–	5.662e-02	–	1.532e+00	–	1.626e+00	–
16	1.129e-02	1.50	2.728e-02	1.05	6.270e-01	1.29	7.277e-01	1.16
32	3.217e-03	1.81	8.850e-03	1.62	2.068e-01	1.60	2.413e-01	1.59
64	8.616e-04	1.90	2.766e-03	1.68	6.191e-02	1.74	7.524e-02	1.68
(Case 2: $x_E = V_E$, $x_e = c_e$)								
n	PressErr(C_E)	Conv.	PressErr(V_E)	Conv.	VelErr(c_e)	Conv.	VelErr(b_e)	Conv.
8	4.356e-02	–	5.520e-02	–	2.651e+00	–	2.677e+00	–
16	2.702e-02	0.69	1.830e-02	1.59	1.332e+00	0.99	1.401e+00	0.93
32	8.829e-03	1.61	5.354e-03	1.77	4.329e-01	1.62	4.525e-01	1.63
64	2.798e-03	1.66	1.481e-03	1.85	1.285e-01	1.75	1.339e-01	1.76
(Case 3: $x_E = C_E$, $x_e = b_e$)								
n	PressErr(C_E)	Conv.	PressErr(V_E)	Conv.	VelErr(c_e)	Conv.	VelErr(b_e)	Conv.
8	3.796e-02	–	5.994e-02	–	2.054e+00	–	2.037e+00	–
16	1.824e-02	1.06	3.153e-02	0.93	1.283e+00	0.68	1.222e+00	0.74
32	5.741e-03	1.67	1.033e-02	1.61	4.520e-01	1.50	4.238e-01	1.53
64	1.612e-03	1.83	3.151e-03	1.71	1.376e-01	1.72	1.287e-01	1.72
(Case 4: $x_E = V_E$, $x_e = b_e$)								
n	PressErr(C_E)	Conv.	PressErr(V_E)	Conv.	VelErr(c_e)	Conv.	VelErr(b_e)	Conv.
8	3.699e-02	–	4.889e-02	–	2.221e+00	–	2.123e+00	–
16	2.368e-02	0.64	1.313e-02	1.90	8.970e-01	1.31	8.320e-01	1.35
32	7.515e-03	1.66	3.230e-03	2.02	2.911e-01	1.62	2.512e-01	1.73
64	2.439e-03	1.62	7.949e-04	2.02	8.887e-02	1.71	7.242e-02	1.79

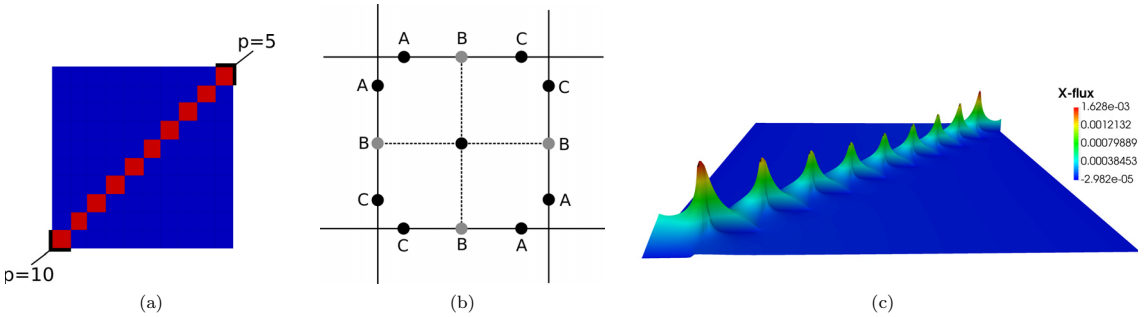

(a) (b) (c)

FIGURE 4. Flux accuracy test: (a) permeability field and boundary conditions; (b) three different sets of positions of the shifted face points for cells on the high permeability diagonal; (c) flux in the x-direction computed on the fine scale.

TABLE 4. Convergence rates on random Voronoi meshes in three-dimensions.

(Case 1: $x_E = C_E$, $x_e = c_e$)								
n	PressErr(C_E)	Conv.	PressErr(V_E)	Conv.	VelErr(c_e)	Conv.	VelErr(b_e)	Conv.
8	7.371e-02	–	9.495e-02	–	6.986e+00	–	7.120e+00	–
16	2.671e-02	1.46	3.461e-02	1.46	3.502e+00	1.00	3.562e+00	1.00
32	7.586e-03	1.82	1.329e-02	1.38	1.636e+00	1.10	1.647e+00	1.11
64	2.016e-03	1.91	5.777e-03	1.20	7.552e-01	1.12	7.707e-01	1.10
(Case 2: $x_E = V_E$, $x_e = c_e$)								
n	PressErr(C_E)	Conv.	PressErr(V_E)	Conv.	VelErr(c_e)	Conv.	VelErr(b_e)	Conv.
8	1.227e-01	–	1.176e-01	–	7.683e+00	–	7.713e+00	–
16	4.176e-02	1.55	3.465e-02	1.76	3.695e+00	1.06	3.792e+00	1.02
32	1.482e-02	1.49	9.737e-03	1.83	1.680e+00	1.14	1.728e+00	1.13
64	6.013e-03	1.30	2.548e-03	1.93	7.613e-01	1.14	7.968e-01	1.12
(Case 3: $x_E = C_E$, $x_e = b_e$)								
n	PressErr(C_E)	Conv.	PressErr(V_E)	Conv.	VelErr(c_e)	Conv.	VelErr(b_e)	Conv.
8	8.705e-02	–	1.092e-01	–	7.781e+00	–	7.432e+00	–
16	3.115e-02	1.48	3.880e-02	1.49	3.901e+00	1.00	3.650e+00	1.03
32	8.613e-03	1.85	1.405e-02	1.47	1.851e+00	1.08	1.679e+00	1.12
64	2.243e-03	1.94	5.882e-03	1.26	8.525e-01	1.12	7.678e-01	1.13
(Case 4: $x_E = V_E$, $x_e = b_e$)								
n	PressErr(C_E)	Conv.	PressErr(V_E)	Conv.	VelErr(c_e)	Conv.	VelErr(b_e)	Conv.
8	1.030e-01	–	9.719e-02	–	7.557e+00	–	7.202e+00	–
16	3.858e-02	1.42	3.108e-02	1.64	3.680e+00	1.04	3.460e+00	1.06
32	1.404e-02	1.46	8.689e-03	1.84	1.724e+00	1.09	1.584e+00	1.13
64	5.886e-03	1.25	2.278e-03	1.93	7.822e-01	1.14	7.138e-01	1.15

compared to a solution computed on a fine scale mesh with 250×250 elements, see Figure 4c for the computed fine scale flux in the x-direction, and Figure 5 for the comparison of the four methods.

The original MFD method, Case B, underestimates the flux on the diagonal, while the modified method computes a more accurate flux, as seen in Case C. The reason is that the velocity is highest near the corners where two high permeability blocks meet, see Figure 4c. The choice of placing the face points near these corners produces a better sampling of the exact flux, thus producing a more accurate average flux on the faces. Furthermore, this improvement does not require refining the mesh and increasing the number of degrees of freedom. We also note that the introduced non-symmetry is restricted to elements on the diagonal and their neighbors. Most of the local matrices remain symmetric and consistent with the original MFD method.

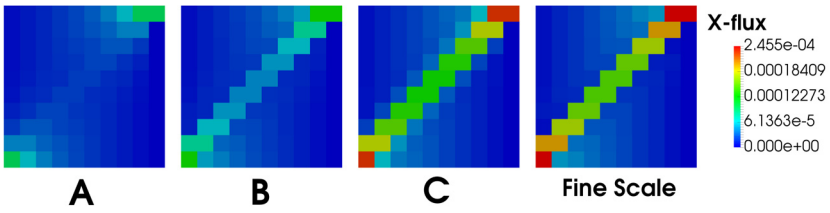

FIGURE 5. Comparison of the flux in x-direction between three shifted face point positions (A, B, C) and a fine scale reference solution (*right*).

The extended space of MFD methods we present can indeed result in more accurate solutions on a given mesh. We note that moving the face points away from the diagonal results in less accurate flux. In practice, advanced knowledge of large scale permeability features could be utilized in the choice of face and element points. Furthermore, the family of MFD methods can be parametrized and searched, which is similar to the approach of M-adaptation for MFD methods [33].

6. Conclusions

The MFD method defines a family of discretizations on a very general set of polyhedral meshes. Solving over general polyhedra allows for better representation of complex geometric features. Special care must be taken when solving for porous media multi-phase flow equations, as they can be sensitive to the kind of discretization used. Methods such as the two-point flux approximation (TPFA) have been well established for such equations. While the original MFD method definition encompasses TPFA over rectangular grids, it does not include TPFA for cases such as Voronoi meshes. We have demonstrated the connection between the MFD method and TPFA over Voronoi grids by defining a generalization of the original MFD method. Establishing this connection results in a reduction of the saddle-point system associated with the MFD method to a symmetric-positive definite system through a Schur complement. In the case of rectangular grids, we have observed that the generalization connects the MFD method with point-centered schemes.

We have presented a proof of stability and convergence of the generalization using tools from MFE methods and standard MFD methods. The analysis suggests that the modification made to the MFD method maintains first-order convergence for both the pressure and velocity unknowns. We have also demonstrated second-order convergence (or superconvergence) of the pressure unknown by employing special lifting operators. In the case of two-dimensional rectangular grids, we explicitly constructed such operators, which can be considered as shape functions for a traditional MFE method. The method corresponds to different choices for the test and trial $H(\Omega;\mathrm{div})$ spaces, or a Petrov–Galerkin type method.

Further connections with methods from the Finite Volume literature should be investigated. This includes various MPFA methods [1] and point-centered schemes [26]. The method defined here might open further possibilities for finding discretization schemes that satisfy the discrete maximum principle [42]. In addition, we plan to extend the theoretical results of this work to include velocity superconvergence and construction of lifting operators for more element types.

The visualization in this work was generated using Paraview scientific visualizer [34]. The code used to produce results was written in Python and uses the NumPy [53], SciPy [36] and Cython [9] libraries. The code uses sparse direct solvers found in spsolve library of SciPy. For larger models, the code has been coupled with PETSc [7] using the petsc4py interface [20]. For cell volume and centroid computations, the code uses the algorithm defined in [44]. The Voronoi diagrams were generated using the Voro++ software package [51].

Appendix A. Quadrature estimate

We demonstrate that the choice of quadrature (2.62) satisfies condition (2.60). For simplicity, we consider first $E = [0,1]^2$. Notice that for a constant vector u_0 on E, denoting $u_{0,E} = (u_0)_E^I$, we have

$$\sigma_E(\bar{K}_E^{-1}; u_{0,E}, v_E) = 0, \tag{A.1}$$

which can be observed by setting $u_0 = (1,0)^T$ and $v_E = (1,0,0,0)$:

$$\int_E \bar{K}_E^{-1} R_E(u_{0,E}) \cdot \tilde{R}_E(v_E)\,\mathrm{d}V = \int_E \bar{K}_E^{-1} \begin{pmatrix} 1 \\ 0 \end{pmatrix} \cdot \begin{pmatrix} W_x w_y \\ 0 \end{pmatrix} \mathrm{d}V = \frac{1-\tilde{x}}{k_x} = [u_{0,E}, v_E]_E.$$

The same argument can be extended to all other combinations of u_0 and v_E. Due to non-symmetry of σ_E, in general

$$\sigma_E(\bar{K}_E^{-1}; v_E, u_{0,E}) \neq 0.$$

However, we can proceed by first defining an operator $\hat{T}_E$,

$$\hat{T}_E = \begin{pmatrix} \hat{w}_x & 0 \\ 0 & \hat{w}_y \end{pmatrix}, \text{ with } \int_e x\hat{w}_x\,\mathrm{d}S = 1 - \tilde{x}, \quad \int_e \hat{w}_x\,\mathrm{d}S = 1,$$

and similarly for $\hat{w}_y$. We now observe that for any v_E and u_0,

$$[v_E, u_{0,E}]_E = \int_E \bar{K}_E^{-1} R_E(v_E) \cdot \hat{T}_E T_E u_0\,\mathrm{d}V, \tag{A.2}$$

since for $v_E = (1,0,0,0)$ and $u_0 = (1,0)^T$ we have

$$\int_E \bar{K}_E^{-1} R_E(v_E) \cdot \hat{T}_E T_E u_0\,\mathrm{d}V = \int_E k_x^{-1} x\hat{w}_x w_y\,\mathrm{d}V = \frac{1-\tilde{x}}{k_x} = [v_E, u_{0,E}]_E,$$

and for $v_E = (0,0,1,0)$ and $u_0 = (1,0)^T$,

$$\int_E \bar{K}_E^{-1} R_E(v_E) \cdot \hat{T}_E T_E u_0\,\mathrm{d}V = \int_E k_x^{-1}(1-x)\hat{w}_x w_y\,\mathrm{d}V = \frac{\tilde{x}}{k_x} = [v_E, u_{0,E}]_E,$$

and similarly for all other combinations of v_E and u_0. We note that for a constant vector $u_0 = (u_0^x, u_0^y)^T$ on any $E \in \mathcal{T}_h$, since

$$\int_E \hat{w}_x\,\mathrm{d}V = \int_E \hat{w}_y\,\mathrm{d}V = |E|, \text{ then } \int_E (\hat{T}_E T_E u_0 - T_E u_0)\,\mathrm{d}V = \int_E \begin{pmatrix} (\hat{w}_x - 1) w_y u_0^x \\ (\hat{w}_y - 1) w_x u_0^y \end{pmatrix} \mathrm{d}V = \begin{pmatrix} 0 \\ 0 \end{pmatrix},$$

and the Friedrichs inequality [11] implies that

$$\|\hat{T}_E T_E u_0 - T_E u_0\|_{(L^2(E))^2} \leq C h_E \|u_0\|_{(L^2(E))^2}. \tag{A.3}$$

Lemma A.1. *The choice of velocity inner product with matrix* (2.62) *satisfies condition* (2.60).

Proof. Given $u \in (H^1(E))^d$ and $v \in (H^1(E))^d$, let $u_E = u_E^I$ and $v_E = v_E^I$. We have

$$\sigma_E(K^{-1}; u_E, v_E) = \sigma_E(\bar{K}_E^{-1}; u_E, v_E) + \int_E (\bar{K}_E^{-1} - K^{-1}) R_E(u_E) \cdot \tilde{R}_E(v_E)\,\mathrm{d}V \equiv \tilde{J}_1 + \tilde{J}_2.$$

Let u_0 and v_0 be the mean values of u and v, respectively, and let $u_{0,E} = (u_0)_E^I$ and $v_{0,E} = (v_0)_E^I$. For $\tilde{J}_1$ we have, using (A.1) and (A.2),

$$\begin{aligned}\tilde{J}_1 &= [u_E, v_E]_E - \int_E \bar{K}_E^{-1} R_E(u_E) \cdot \tilde{R}_E(v_E)\,\mathrm{d}V,\\ &= [u_E - u_{0,E}, v_E - v_{0,E}]_E - \int_E \bar{K}_E^{-1} R_E(u_E - u_{0,E}) \cdot (\tilde{R}_E(v_E) - \hat{T}_E T_E v_0)\,\mathrm{d}V\\ &= [u_E - u_{0,E}, v_E - v_{0,E}]_E - \int_E \bar{K}_E^{-1} R_E(u_E - u_{0,E}) \cdot \tilde{R}_E(v_E - v_{0,E})\,\mathrm{d}V\\ &\quad - \int_E \bar{K}_E^{-1} R_E(u_E - u_{0,E}) \cdot (T_E v_0 - \hat{T}_E T_E v_0)\,\mathrm{d}V.\end{aligned}$$

Using Lemmas 2.11, and 2.12, (A.3) and (2.50), we obtain

$$|\tilde{J}_1| \le C h_E^2 \|u\|_{(H^1(E))^2} \|v\|_{(H^1(E))^2}.$$

Expression $\tilde{J}_2$ can be divided into

$$\begin{aligned}\tilde{J}_2 &= \int_E (\bar{K}_E^{-1} - K^{-1}) R_E(u_E - u_{0,E}) \cdot \tilde{R}_E(v_E)\,\mathrm{d}V + \int_E (\bar{K}_E^{-1} - K^{-1}) R_E(u_{0,E}) \cdot \tilde{R}_E(v_E - v_{0,E})\,\mathrm{d}V\\ &\quad + \int_E (\bar{K}_E^{-1} - K^{-1}) R_E(u_{0,E}) \cdot \tilde{R}_E(v_{0,E})\,\mathrm{d}V \equiv \tilde{J}_{21} + \tilde{J}_{22} + \tilde{J}_{23}\end{aligned}$$

We can bound $\tilde{J}_{21} + \tilde{J}_{22}$ using (2.7), (2.40)–(2.41) and (2.53),

$$|\tilde{J}_{21} + \tilde{J}_{22}| \le C h_E^2 \|v\|_{(H^1(E))^2} \|u\|_{(H^1(E))^2}.$$

For expression $\tilde{J}_{23}$, setting $\overline{K^{-1}T_E} = \frac{1}{|E|}\int_E K^{-1} T_E$ and using (2.6), we have

$$\begin{aligned}|\tilde{J}_{23}| &= \left| \int_E (\bar{K}_E - K) \bar{K}_E^{-1} u_0 \cdot K^{-1} T_E v_0\,\mathrm{d}V \right| = \left| \int_E (\bar{K}_E - K) \bar{K}_E^{-1} u_0 \cdot (K^{-1} T_E - \overline{K^{-1} T_E}) v_0\,\mathrm{d}V \right|\\ &\le C h_E^2 \|u\|_{(L^2(E))^2} \|v\|_{(L^2(E))^2}.\end{aligned}$$

Combining the above expressions gives the desired result. □

Acknowledgements. The authors acknowledge the financial support from the King Abdullah University of Science and Technology Academic Excellence Alliance, from Saudi Aramco and from the Center for Subsurface Modeling Industrial Affiliates. The second author was partially supported by DOE Grant DE-FG02-04ER25617; the third author was partially supported by DOE Grant DE-FG02-04ER25618 and NSF Grant DMS 1418947. We also acknowledge helpful feedback from Todd Arbogast, Mojdeh Delshad, Leszek Demkowicz, Xin Yang, Guangri (Gary) Xue and Jerome Droniou.

References

[1] I. Aavatsmark, An introduction to multipoint flux approximations for quadrilateral grids. *Comput. Geosci.* **6** (2002) 405–432.
[2] J. Aghili, S. Boyaval and D. Di Pietro, Hybridization of mixed high-order methods on general meshes and application to the stokes equations. *Comput. Methods Appl. Math.* **15** (2015) 111–134.
[3] S. Agmon, Lectures on elliptic boundary value problems. Vol. 2. American Mathematical Soc. (2010).
[4] T. Arbogast, M. Wheeler and I. Yotov, Mixed finite elements for elliptic problems with tensor coefficients as cell-centered finite differences. *SIAM J. Numer. Anal.* **34** (1997) 828–852.
[5] T. Arobogast, C. Dawson, P. Keenan, M. Wheeler and I. Yotov, Enhanced cell-centered finite differences for elliptic equations on general geometry. *SIAM J. Scientific Comput.* **19** (1998) 404–425.
[6] K. Aziz, Reservoir simulation grids: Opportunities and problems. *J. Petroleum Technol.* (1993) 658–663

[7] S. Balay, M. Adams, J. Brown, P. Brune, K. Buschelman, V. Eijkhout, W.D. Gropp, D. Kaushik, M. Knepley, L. McInnes, K. Rupp, B. Smith and H. Zhang, PETSc Web page, http://www.mcs.anl.gov/petsc (2014).

[8] J. Baranger, J.-F. Maitre and F. Oudin, Connection between finite volume and mixed finite element methods. *RAIRO-Modél. Math. Anal. Numér.* **30** (1996) 445–465.

[9] S. Behnel, R. Bradshaw, C. Citro, L. Dalcin, D. Seljebotn and K. Smith, Cython: The best of both worlds. *Comput. Sci. Eng.* **13** (2011) 31–39.

[10] P. Berry, S Bonduá, V. Bortolotti, C. Cormio and E.M. Vasini, A gis-based open source pre-processor for georesources numerical modeling. *Environ. Model. Softw.* **62** (2014) 52–64.

[11] S. Brenner and L. Scott, *The Mathematical Theory of Finite Element Methods*. Springer, 2nd edition (2002).

[12] F. Brezzi and M. Fortin, *Mixed and hybrid finite element methods*. Springer-Verlag, New York (1991).

[13] F. Brezzi, J. Douglas Jr and L. Marini, Two families of mixed finite elements for second order elliptic problems. *Numer. Math.* **47** (1985) 217–235.

[14] F. Brezzi, K. Lipnikov and M. Shashkov, Convergence of the mimetic finite difference method for diffusion problems on polyhedral meshes. *SIAM J. Numer. Anal.* **43** (2005) 1872–1896.

[15] F. Brezzi, K. Lipnikov and V. Simoncini, A family of mimetic finite difference methods on polygonal and polyhedral meshes. *Math. Models Methods Appl. Sci.* **15** (2005) 1533–1551.

[16] F. Brezzi, R. S, Falk and L. D, Marini. Basic principles of mixed virtual element methods. *ESAIM: M2AN* **48** (2014) 1227–1240.

[17] A. Cangiani and G. Manzini, Flux reconstruction and solution post-processing in mimetic finite difference methods. *Comput. Methods Appl. Mech. Engrg.* **197** (2008) 933–945.

[18] B. Cockburn, J. Gopalakrishnan and R. Lazarov, Unified hybridization of discontinuous galerkin, mixed, and continuous galerkin methods for second order elliptic problems. *SIAM J. Numer. Anal.* **47** (2009) 1319–1365.

[19] L. da Veiga, F. Brezzi, A. Cangiani, G. Manzini, L. Marini and A. Russo, Basic principles of virtual element methods. *Math. Models Methods Appl. Sci.* **23** (2013) 199–214.

[20] L. Dalcin, petsc4py. https://code.google.com/p/petsc4py/ (2013).

[21] D.A. Di Pietro, A. Ern and S. Lemaire, An arbitrary-order and compact-stencil discretization of diffusion on general meshes based on local reconstruction operators. *Comput. Methods Appl. Math.* **14** (2014) 461–472.

[22] J. Douglas Jr and J. Wang, Superconvergence of mixed finite element methods on rectangular domains. *Calcolo* **26** (1989) 121–133.

[23] J. Droniou, R. Eymard, T. Gallouët and R. Herbin, A unified approach to mimetic finite difference, hybrid finite volume and mixed finite volume methods. *Math. Models Methods Appl Sci.* **20** (2010) 265–295.

[24] J. Droniou, R. Eymard, T. Gallouët and R. Herbin, Gradient schemes: a generic framework for the discretisation of linear, nonlinear and nonlocal elliptic and parabolic equations. *Math. Models Methods Appl. Sci.* **23** (2013) 2395–2432.

[25] M. Edwards, Unstructured, control-volume distributed, full-tensor finite-volume schemes with flow based grids. *Comput. Geosci.* **6** (2002) 433–452.

[26] M. Edwards and C. Rogers, Finite volume discretization with imposed flux continuity for the general tensor pressure equation. *Comput. Geosci.* **2** (1998) 259–290.

[27] R. Ewing, R. Lazarov and J. Wang, Superconvergence of the velocity along the gauss lines in mixed finite element methods. *SIAM J. Numer. Anal.* **28** (1991) 1015–1029.

[28] R. Eymard, T. Gallouët and R. Herbin, Finite volume methods. Vol. VII of *Handbook of Numerical Analysis*. North-Holland, Amsterdam (2000).

[29] C.M. Freeman, K.L. Boyle, M. Reagan, J. Johnson, C. Rycroft and G.J. Moridis, Meshvoro: A three-dimensional voronoi mesh building tool for the tough family of codes. *Comput. Geosci.* **70** (2014) 26–34.

[30] L.S.K. Fung *et al.*, Parallel unstructured-solver methods for simulation of complex giant reservoirs. *SPE J.* **13** (2008) 440–446.

[31] V. Girault and P.-A. Raviart, Finite Element Methods for Navier-Stokes Equations. Number 5 in *Springer series in Computational Mathematics*. Springer-Verlag (1986).

[32] P. Grisvard, *Elliptic problems in nonsmooth domains*. Vol. 69. SIAM (2011).

[33] V. Gyrya, K. Lipnikov, G. Manzini and D. Svyatskiy, M-adaptation in the mimetic finite difference method. *Math. Models Methods Appl. Sci.* **24** (2014) 1621–1663.

[34] A. Henderson, The paraview guide: A parallel visualization application. kitware inc. Technical report (2007).

[35] R. Ingram, M. Wheeler and I. Yotov, A multipoint flux mixed finite element method on hexahedra. *SIAM J. Numer. Anal.* **48** (2010) 1281–1312.

[36] E. Jones *et al.*, SciPy: Open source scientific tools for Python (2001).

[37] R. Klausen and A. Stephansen, Convergence of multi-point flux approximation on general grids and media. *Int. J. Numer. Anal. Model.* **9** (2012) 584–606.

[38] R. Klausen and R. Winther, Convergence of multipoint flux approximations on quadrilateral grids. *Numer. Methods Partial Differ. Eq.* **22** (2006) 1438–1454.

[39] R. Klausen and R. Winther, Robust convergence of multi point flux approximation on rough grids. *Numer. Math.* **104** (2006) 317–337.

[40] Y. Kuznetsov and S. Repin, New mixed finite element method on polygonal and polyhedral meshes. *Russian J. Numer. Anal. Math. Model.* **18** (2003) 261–278.

[41] K. Lipnikov, M. Shashkov and I. Yotov, Local flux mimetic finite difference methods. *Numer. Math.* **112** (2009) 115–152.

[42] K. Lipnikov, G. Manzini and D. Svyatskiy, Analysis of the monotonicity conditions in the mimetic finite difference method for elliptic problems. *J. Comput. Phys.* **230** (2011) 2620–2642.

[43] K. Lipnikov, G. Manzini and M. Shashkov, Mimetic finite difference method. Physics-compatible numerical methods. *J. Comput. Phys.* **257** (2014) 1163–1227.

[44] B. Mirtich, Fast and accurate computation of polyhedral mass properties. *J. Graphics Tools* **1** (1996) 31–50.

[45] L. Mu, J. Wang and X. Ye, Weak galerkin finite element methods on polytopal meshes. *Int. J. Numer. Anal. Model.* **12** (2015) 536–566.

[46] M. Nakata, A. Weiser and M. Wheeler, Some superconvergence results for mixed finite element methods for elliptic problems on rectangular domains. *The Mathematics of Finite Elements and Applications V*, edited by J.R. Whiteman. Academic Press, London (1985) 367–389.

[47] C. Palagi and K. Aziz, Use of Voronoi grid in reservoir simluation. *SPE Adv. Technol. Ser.* **2** (1994) 69–77.

[48] S. Panday, C.D. Langevin, R.G. Niswonger, M. Ibaraki and J.D. Hughes, Modflow-usg version 1: An unstructured grid version of MODFLOW for simulating groundwater flow and tightly coupled processes using a control volume finite-difference formulation. Technical report, US Geological Survey (2013).

[49] P. Raviart and J. Thomas, A mixed finite element method for 2-nd order elliptic problems. In *Mathematical Aspects of Finite Element Methods*. Springer (1977) 292–315.

[50] T. Russell and M. Wheeler, Finite element and finite difference methods for continuous flows in porous media. In Vol. 1 of *Mathematics of Reservoir Simulation, Frontiers in Applied Mathematics*, edited by R.E. Ewing. SIAM (1983).

[51] C. Rycroft, Voro++: A three-dimensional voronoi cell library in c++ (2009).

[52] Schlumberger Geoquest, Eclipse 100 reference manual. Schlumberger Geoquest (2001).

[53] S. Van Der Walt, S. Colbert and G. Varoquaux, The numpy array: a structure for efficient numerical computation. *Comput. Sci. Eng.* **13** (2011) 22–30.

[54] M. Vohralík and B. Wohlmuth, Mixed finite element methods: implementation with one unknown per element, local flux expressions, positivity, polygonal meshes, and relations to other methods. *Math. Models Methods Appl. Sci.* **23** (2013) 803–838.

[55] A. Weiser and M. Wheeler, On convergence of block-centered finite differences for elliptic problems. *SIAM J. Numer. Anal.* **25** (1988) 351–375.

[56] M. Wheeler, G. Xue and I. Yotov, A multipoint flux mixed finite element method on distorted quadrilaterals and hexahedra. *Numer. Math.* **121** (2012) 165–204.

[57] M. Wheeler and I. Yotov, A multipoint flux mixed finite element method. *SIAM J. Numer. Anal.* **44** (2006) 2082–2106.